The Astrophysical Journal, 920:146 (18pp), 2021 October 20 https://doi.org/10.3847/1538-4357/ac1865

Empirically Determining Substellar Cloud Compositions in the Era of the James Webb Space Telescope

Jessica L. Luna[1] and Caroline V. Morley
Department of Astronomy, The University of Texas at Austin, 2515 Speedway Stop C1402 Austin, TX 78712-1206, USA; jessicaluna@utexas.edu
Received 2021 April 12; revised 2021 July 21; accepted 2021 July 22; published 2021 October 25

Abstract

Most brown dwarfs have atmospheres with temperatures cold enough to form clouds. A variety of materials likely condense, including refractory metal oxides and silicates; the precise compositions and crystal structures of predicted cloud particles depend on the modeling framework used and have not yet been empirically constrained. Spitzer has shown tentative evidence of the silicate feature in L dwarf spectra and the James Webb Space Telescope (JWST) can measure these features in many L dwarfs. Here, we present new models to predict the signatures of the strongest cloud absorption features. We investigate different cloud mineral species and determine how particle size, mineralogy, and crystalline structure change spectral features. We find that silicate and refractory clouds have a strong cloud absorption feature for small particle sizes ($\leqslant 1$ μm). Model spectra are compared to five brown dwarfs that show evidence of the silicate feature; models that include small particles in the upper layers of the atmosphere produce a broad cloud mineral feature, and that better match the observed spectra than the Ackerman & Marley cloud model. We simulate observations with the Mid-Infrared Instrument (MIRI) instrument on JWST for a range of nearby, cloudy brown dwarfs, demonstrating that these features could be readily detectable if small particles are present. Furthermore, for photometrically variable brown dwarfs, our predictions suggest that with JWST, by measuring spectroscopic variability inside and outside a mineral feature, we can establish silicate (or other) clouds as the cause of variability. Mid-infrared spectroscopy is a promising tool to empirically constrain the complex cloud condensation sequence in brown dwarf atmospheres.

Unified Astronomy Thesaurus concepts: Brown dwarfs (185); L dwarfs (894); Stellar atmospheres (1584); Extrasolar gaseous giant planets (509); Exoplanet atmospheres (487)

1. Introduction

Brown dwarfs are substellar objects that are too small in mass to fuse hydrogen. Their cool atmospheres are analogous in both temperature and composition to gas giant planets. Brown dwarfs cool as they age and their temperatures determine the species that can condense to form clouds in their atmospheres. For L dwarfs (>1300 K), layers of thick silicate and refractory clouds likely form (Tsuji et al. 1996; Allard et al. 2001; Marley et al. 2002; Burrows et al. 2006; Cushing et al. 2008). As brown dwarfs cool, these clouds appear to clear significantly at the L/T transition (≈1200 K). For late-T dwarfs (<1000 K), sulfide and salt clouds can condense (Visscher et al. 2006; Morley et al. 2012). For the coldest Y dwarfs, water ice and ammonia clouds can form (Burrows et al. 2003; Morley et al. 2014). Clouds have a substantial impact on brown dwarf spectra, and 25 yr after the discoveries of the first known brown dwarfs, modeling these clouds accurately in detail remains one of the largest uncertainties in brown dwarf astrophysics (Marley et al. 2013; Marley & Robinson 2015).

1.1. Approaches to Cloud Modeling

We will briefly review the three major classes of brown dwarf cloud models and highlight the cloud species predicted by each. These models can differ significantly in the clouds that form, their masses, number densities, size distributions, and the resulting impact on the spectra.

One straightforward approach, *rainout equilibrium* (Chabrier & Baraffe 2000; Allard et al. 2001), adopts equilibrium chemistry to predict condensation. This approach has the advantage of not requiring knowledge of microphysical processes that are challenging to model from first principles with many uncertain physical quantities. Rainout equilibrium calculations use a *bottom-up* approach to the chemistry of cloud formation, assuming that the atmosphere is in thermochemical equilibrium but removing material from the gas phase as materials condense (Lodders & Fegley 2006; Marley et al. 2013). The cloud locations and particle sizes are determined by balancing the downward transport of particles by sedimentation with the upward mixing of vapor and condensate (Ackerman & Marley 2001; Saumon & Marley 2008; Stephens et al. 2009; Morley et al. 2012, hereafter AM01). It has yet to be determined if every possible species does condense in the predicted sequence. Some species may have barriers to their formation (e.g., slow nucleation timescales) that are not modeled in this framework, which assumes that all vapor in excess of the saturation vapor pressure condenses.

A second approach to cloud modeling uses grain chemistry by treating cloud formation as a kinetic process using a *top-down* approach (Helling et al. 2008a, 2008b). They start with TiO_2 seed particles at the top of the atmosphere and follow their growth as they fall downward, modeling the heterogeneous chemical reactions occurring on their surfaces. These seed particles accrete condensate material and grow, which results in *dirty grains* with mixed compositions. The resulting clouds can be different in composition, location, and particle size distributions than rainout equilibrium. For example, Helling & Woitke (2006) predict that SiO_2 condenses, which is not predicted from equilibrium chemistry calculations for a solar composition atmosphere.

[1] NSF Graduate Research Fellow.

A microphysical framework developed for the solar system but recently used for exoplanets and brown dwarfs is Community Aerosol & Radiation Model for Atmospheres (CARMA). CARMA attempts to model microphysical processes from first principles using a bin scheme approach to fully resolve particle size distributions (Turco et al. 1979; Toon et al. 1988; Ackerman et al. 1995; Gao & Benneke 2018; Gao et al. 2018; Powell et al. 2018, 2019). It treats the microphysical processes of nucleation (heterogeneous and homogeneous), condensation, evaporation, and coagulation, and vertical transport by atmospheric mixing and gravitational settling.

Modeling microphysics is challenging due to the plethora of unknowns that are required as inputs. They require assumptions about properties that are unknown, including vertical mixing rates, material properties like surface tension, and the detailed knowledge of formation pathways. The resulting clouds are broadly similar to equilibrium condensation clouds but differ in particle sizes and locations (Gao et al. 2018).

1.2. Directly Observing Cloud Properties

With different models resulting in a range of cloud properties, and some models not requiring clouds at all, a key next step is to empirically test our approaches by measuring cloud properties directly for an ensemble of brown dwarfs. Some tentative evidence from Spitzer Infrared Spectrograph (IRS) suggests that silicate features are present in L dwarf spectra but with smaller particle sizes than produced by AM01 (Cushing et al. 2006; Helling & Woitke 2006; Looper et al. 2008). Further evidence also suggests that some brown dwarfs have small (submicron) grain in their photospheres: Hiranaka et al. (2016) showed that small submicron-sized grains above the main cloud deck can explain the near-IR (NIR) colors of red L dwarfs. They conclude that brown dwarf models should include both large and small (submicron) sized particles to reproduce the spectra of red L dwarfs.

The MIRI instrument on board the James Webb Space Telescope (JWST) will allow us to measure cloud mineral spectral features in many L dwarfs, allowing us to investigate cloud compositions, particle sizes, and mineral structures, as well as the impact of these clouds on variability. These observations will provide the strongest direct evidence of cloud formation and allow us to determine which cloud modeling frameworks best capture the physics of brown dwarf atmospheres.

In this paper, we investigate the effect clouds have on the observed thermal emission spectra of brown dwarf atmospheres. In particular, we focus on clouds present in L dwarfs, where the atmospheres are dominated by silicate and other refractory clouds. We present new theoretical models for brown dwarf atmospheres motivated by observational results, including small particles to produce cloud spectral features. We discuss the properties of our model in Section 2. In Section 3, we show the results of our model thermal emission spectra and in Section 4 we fit models to Spitzer IRS observations and simulate JWST observations. Finally, in Section 5, we discuss the implications of our new cloud models and in Section 6 we conclude.

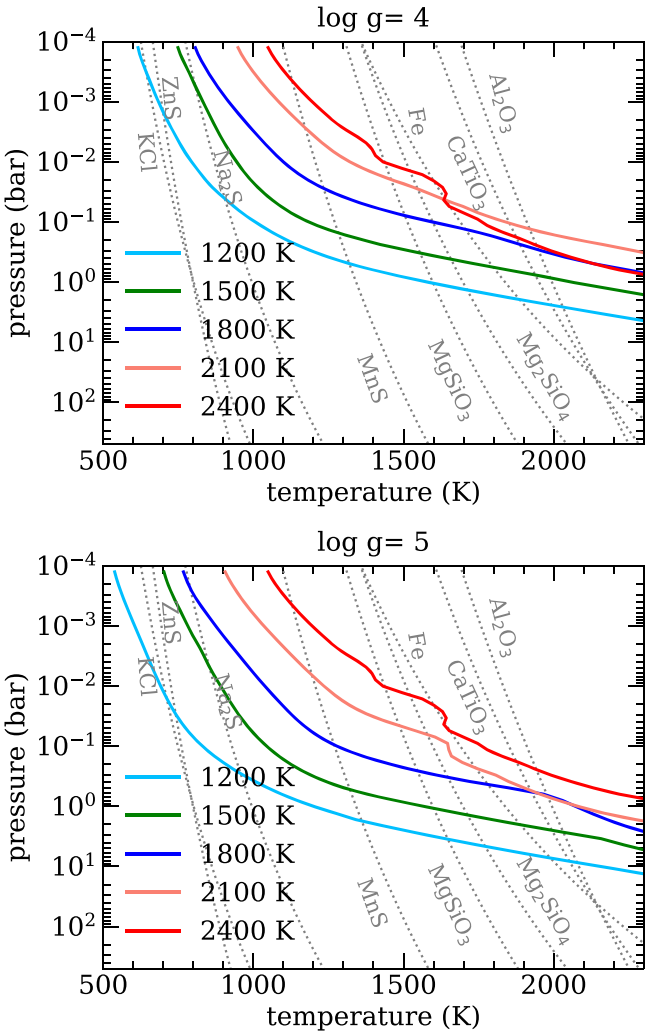

Figure 1. Pressure–temperature profiles for models with log $g = 4$ (top) and log $g = 5$ (bottom). We compute these atmosphere models assuming radiative-convective equilibrium.

2. Methods

We used a series of 1D models to investigate the effect that clouds can have on thermal emission spectra of unirradiated substellar objects.

2.1. Atmosphere Models

We calculate the temperature structures of model atmospheres assuming radiative-convective equilibrium. The atmosphere models are described in detail by McKay et al. (1989), Marley et al. (1996, 1999, 2002), Burrows et al. (1997), Fortney et al. (2008), Saumon & Marley (2008), and Morley et al. (2012, 2014). The opacity database for gases is described in Freedman et al. (2008, 2014). We ran a small grid to explore a range in effective temperatures of 1200–2400 K and log $g = 4$ and log $g = 5$ as shown in Figure 1. These models include *standard* brown dwarf clouds (forsterite, iron, and corundum) using the AM01 cloud to determine cloud locations and particle sizes, assuming a sedimentation efficiency $f_{\rm sed} = 2$.

2.2. Ad hoc Cloud Model

Since the standard brown dwarf cloud models do not include the small particles required to match observations we invoke an

ad hoc cloud layer to control the size, locations, and number density of particles. We insert our ad hoc cloud layer at a pressure level where we expect these silicate clouds could be present, at lower pressures than the AM01 cloud.

As in the AM01 cloud model, we use a log-normal size distribution of particles defined as

$$\frac{dn}{dr} = \frac{N}{r\sqrt{2\pi}\,\ln\sigma}\exp\left[-\frac{\ln^2(r/r_g)}{2\ln^2\sigma}\right], \quad (1)$$

where N is the total number of particles, σ is the standard deviation of the log-normal distribution, and r_g is the geometric mean radius. σ represents the width of the log-normal distribution of particles. For this study, we use a narrow distribution of particle sizes ($\sigma = 1.2$). As σ approaches 1, the distribution of particles sizes decreases until r equals the geometric mean radius and Equation (1) reduces to the Dirac-delta function. By setting $\sigma = 1.2$, we average over unphysical Mie scattering effects for a single particle size while ensuring that the majority of particles will be close to the mode radius.

We assume a constant number density of ad hoc cloud particles in each layer by setting the ratio of cloud particle number density, $n_{\rm cloud}$, to gas number density, n, in each atmospheric layer as a constant ($c = n_{\rm cloud}/n$). The constant, c, is defined as

$$c = \frac{\tau_{\rm cloud}}{\pi\, r_{\rm eff}^2 \sum n \Delta z}, \quad (2)$$

where $r_{\rm eff}$ is the effective (area-weighted) radius, $\tau_{\rm cloud}$ is the ad hoc cloud optical depth summed over all layers, and n and Δz are respectively the number density of molecules and vertical height of an atmospheric layer. The effective radius[2] is defined as

$$r_{\rm eff} = r_g \exp[5\ln^2\sigma/2]. \quad (3)$$

The number density of molecules, n, in each layer is found using the pressure and temperature of each atmospheric layer assuming the ideal gas law. We create a marginally optically thick ad hoc cloud ($\tau_{\rm cloud} = 2/3$), where we set the total cloud optical depth for 1 μm particles to $\tau_{\rm cloud,1\ \mu m} = 0.67$ for amorphous particles. For crystalline particles, we scaled down the optical depth to $\tau_{\rm cloud,1\ \mu m} = 0.2$ to better match the amplitude of features observed in the Spitzer/IRS spectra. To determine the number density of cloud particles for larger and smaller particle sizes we scale the number density for 1 μm particles by

$$n_{\rm scaled} = n\left(\frac{r_{\rm v}}{r_{\rm v}(1\ \mu{\rm m})}\right)^{-3}, \quad (4)$$

where $r_{\rm v}$ is the volume averaged radius defined as

$$r_{\rm v} = r_g \exp[3\ln^2\sigma/2]. \quad (5)$$

We keep the total mass of cloud material constant across different particle sizes with the mass density of the cloud material, M, defined as

$$M = (4/3)\,\pi\, r_{\rm v}^3\, \rho_{\rm material}\, n_{\rm cloud}. \quad (6)$$

[2] Hansen & Travis (1974) derive the effective radius for a log-normal size distribution (Equation (2.53)).

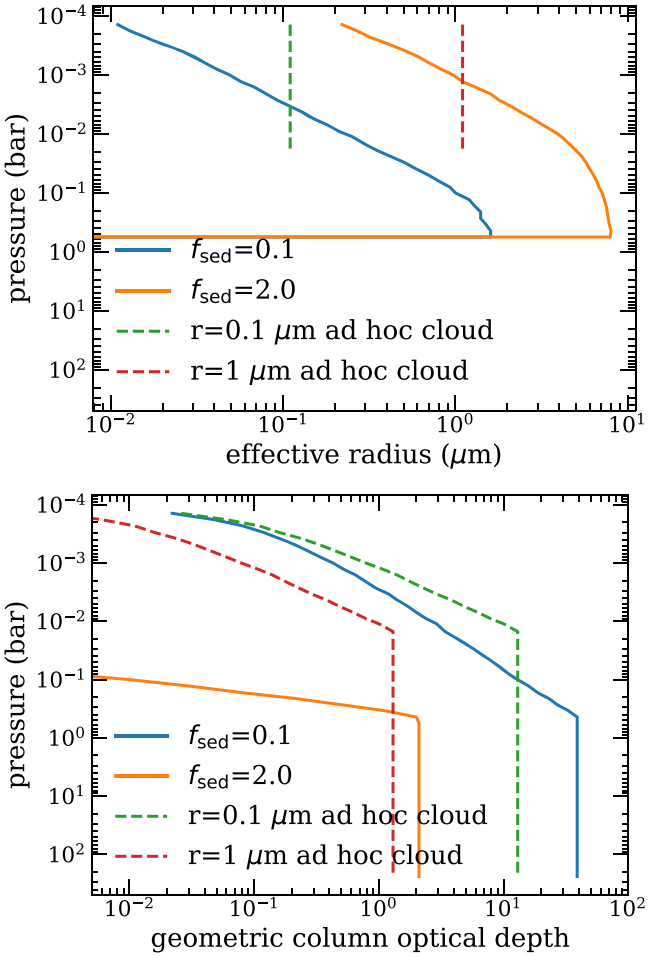

Figure 2. Using forsterite as an example, we compare our ad hoc cloud model (red and green) with the AM01 cloud model for $f_{\rm sed}$ values of 0.1 and 2. The top panel shows the effective radius at each pressure level and the bottom shows the geometric column optical depth. The ad hoc cloud falls in the parameter space of the AM01 cloud model. The ad hoc cloud is marginally optically thick ($\tau \sim 2/3$) with small particles.

Here, $\rho_{\rm material}$, is the density of the cloud particle. For an 1800 K, log $g = 5$ model atmosphere, the mass of a 1 μm amorphous ad hoc forsterite cloud is $M = 5.3 \times 10^{-4}$ g cm^{-2}, which is 16% of the total forsterite cloud.

We compare the properties of the ad hoc cloud with the AM01 model. We compute two models setting the sedimentation efficiency parameter, $f_{\rm sed}$, to 0.1 and 2. A smaller $f_{\rm sed}$ leads to vertically taller clouds with smaller particles and a larger $f_{\rm sed}$ results in thin clouds with larger particles. We show the effective radius and optical depth at each pressure level for the three cloud models in Figure 2. Although the $f_{\rm sed} = 0.1$ model produces small particles in the upper layers of the atmosphere, the resulting cloud becomes optically thick at 1.6 mbar, leading to models with blackbody-like spectra in the NIR that do not match observations of L dwarfs.

2.3. Mie Scattering

We use Mie scattering theory to calculate the absorption and scattering coefficients of particles in the atmosphere for each cloud species independently. We calculate Mie scattering coefficients for particle sizes ranging from 0.001–10 μm.

We use optical properties of each cloud species from the literature summarized in Table 1. A few condensates have

Table 1
Compilation of Optical Constants for Potential Condensates in Brown Dwarf and Gas Giant Exoplanets

Condensate	Name	Comments	References	λ (μm)
Al_2O_3	Corundum	Amorphous; 873K	Begemann et al. (1997)	7.8–500
Al_2O_3	Corundum	Crystalline	Koike et al. (1995)	0.2–12
$CaTiO_3$	Perovskite	Crystalline	Ueda et al. (1998)	0.02–2
			Posch et al. (2003)	2–5843
Fe_2O_3	Hematite	Crystalline	A.H.M.J. Triaud[a]	0.1–1000
Mg_2SiO_4	Forsterite	Amorphous (sol–gel)	Jäger et al. (2003)	0.2–500
Mg_2SiO_4[b]	Forsterite	Crystalline; 295 K	Mutschke & Mohr (2019)	45–500
$MgFeSiO_4$	Olivine	Amorphous (glassy)	Dorschner et al. (1995)	0.19–500
$Mg_{0.8}Fe_{1.2}SiO_4$	Olivine	Amorphous (glassy)	Dorschner et al. (1995)	0.19–500
Fe_2SiO_4	Fayalite	Crystalline	Fabian et al. (2001) [a]	2–200
$MgSiO_3$	Enstatite	Amorphous (sol–gel)	Jäger et al. (2003)	0.2–500
$MgSiO_3$	Enstatite	Amorphous (glassy)	Dorschner et al. (1995)	0.19–500
$MgSiO_3(Mg_2Si_2O_6)$[b]	Enstatite	Crystalline	Jäger et al. (1998)	2–100
$Mg_{0.8}Fe_{0.2}SiO_3$	Pyroxene	Amorphous (glassy)	Dorschner et al. (1995)	0.19–500
$Mg_{0.5}Fe_{0.5}SiO_3$	Pyroxene	Amorphous (glassy)	Dorschner et al. (1995)	0.19–500
$Mg_{0.4}Fe_{0.6}SiO_3$	Pyroxene	Amorphous (glassy)	Dorschner et al. (1995)	0.19–500
$Mg_{0.92}Fe_{0.09}SiO_3$[b]	Orthoenstatite	Crystalline; 10 K, 300 K, 928 K	Zeidler et al. (2015)	5–60
SiO		Amorphous	Palik (1985)	0.05–0.8
			Wetzel et al. (2013)	2–100
SiO_2	Quartz	Amorphous; 300 K	Palik (1985)	0.05–8.4
			Henning & Mutschke (1997)	2–500
SiO_2	Quartz	Crystalline; 928 K	Palik (1985)	0.05–8.4
			Zeidler et al. (2013)	5–50

Notes.
[a] Database of Optical Constants for Cosmic Dust, Laboratory Astrophysics Group of the AIU Jena (http://www.astro.uni-jena.de/Laboratory/OCDB/index.html).
[b] Computed by averaging absorption and scattering efficiencies from three crystallographic axes.

optical properties taken from multiple sources (SiO, amorphous SiO_2, and crystalline SiO_2). The amorphous and crystalline SiO_2 data sets were combined as described in Section 4 of Kitzmann & Heng (2018). To combine the data, the overlapping IR data is replaced with the most recent publication, and the Kramers–Kronig relation is used to combine the IR and short-wavelength data. For SiO, Section 4.1 in Wetzel et al. (2013) describes how the UV–visible data is taken from Palik (1985) ($\lambda < 0.8$ μm), and from 0.8–8 μm a Brendel-oscillator model is fit to experimental results.

To capture sharper crystalline optical constants, we change the resolution of the optical properties from the 196 wavelength point grids used in prior AM01 models (e.g., Saumon & Marley 2008; Morley et al. 2012) to a new 1000 wavelength point grid that ranges from 0.2–230 μm. In Figure 3 we show the optical properties for crystalline enstatite ($Mg_2Si_2O_6$) to illustrate the resolution of these models compared to prior works.

Using the complex refractive indices, we calculate the absorption and scattering efficiency for a range of particle sizes which we show in Figure 4. These coefficients show which wavelengths strongly exhibit Mie scattering features. In Figure 5, we show the absorption and scattering efficiencies for a broad range of condensates that can form in brown dwarf and giant exoplanets. Crystalline structures have refractive indices that are different for each crystallographic axis. To combine information from the three axes into our 1D cloud model, we calculate the absorption and scattering efficiencies for each crystallographic axes separately, then averaged the efficiencies to combine the information (Steyer 1974; Jäger et al. 1998), shown in Figure 5. We find that the numerical calculation approaches the analytic expression for $r \ll \lambda$: at $r \leqslant 0.1$ μm (van de Hulst 1957).

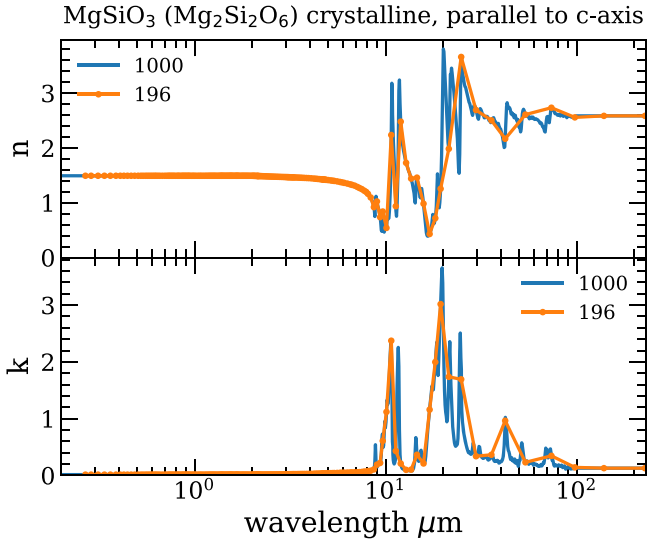

Figure 3. The optical properties for crystalline $MgSiO_3$ ($Mg_2Si_2O_6$) shown with the 196 and 1000 point wavelength grid.

2.4. Thermal Emission Spectra

Using the cloud model and the pressure–temperature profile as inputs, we use the radiative transfer model developed in Morley et al. (2015) to calculate thermal emission spectra. This model calculates the intensity and fluxes in multiple-scattering and emitting layered atmospheres. It takes the optical depth, single scattering albedo, and asymmetry parameter from the cloud model and calculates the flux at a given wavenumber using the C version of the open-source radiative transfer code `disort` (Stamnes et al. 1988; Buras et al. 2011). The radiative

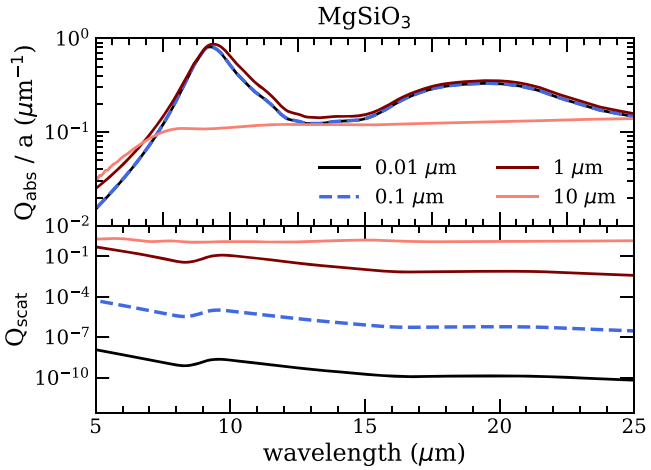

Figure 4. The optical properties for amorphous enstatite ($MgSiO_3$) for a range of particle sizes. We see a peak in absorption around the silicate feature for particles ~1 μm or less, and nearly featureless absorption for 10 μm particles.

transfer code implements the discrete-ordinate method for unpolarized light through a vertically inhomogeneous media.

3. Results

In the following section, we discuss the impacts of silicate and refractory clouds on model spectra of brown dwarfs. Then, we discuss the observability of these features in the near future using JWST simulations and determine the best targets for future observations.

3.1. Model Spectra

In Figures 6 and 7, we show spectra for each of our cloud mineral species. We show an 1800 K, log $g = 5$ model spectrum for the silicate and quartz species and a 2400 K, log $g = 5$ model spectrum for the high-temperature species as representative examples. In Figure 6, we show the wavelength-dependent brightness temperature and pressure. This figure allows us to estimate which average pressure is probed at each wavelength. We compare to a cloud-free model and a standard cloudy ($f_{sed} = 2$, AM01) model. In models with a low-pressure ad hoc cloud, the mid-IR flux is emitted from lower pressures in the atmosphere where the silicate clouds are placed. We show the mid-IR thermal emission spectra in Figure 7 for the same set of models.

To more easily visualize the impact of each cloud species on its corresponding thermal emission spectrum, we define two quantities: flux ratio and amplitude difference.

3.2. Flux Ratios

To determine how the varying cloud optical depth with wavelength changes with spectra, for each model atmosphere, we run a corresponding model, F_{gray}, where the cloud optical depth $\tau(\lambda)$, single scattering albedo ω_o and asymmetry parameter g_o is taken to be the average optical depth $\overline{\tau}$, average single scattering albedo $\overline{\omega_o}$ and average asymmetry parameter $\overline{g_o}$ from 8–18 μm. This wavelength range covers the cloud mineral absorption features for silicates and refractory condensates. We plot the ratio of the cloudy model to the model with the gray cloud,

$$F_{\rm ratio} = \frac{F_{\rm gray}}{F_{\rm cloud}}. \quad (7)$$

The flux ratio allows us to determine the wavelengths of the strongest non-gray mineral features and systematically identify how that feature changes with respect to particle size and composition.

Each cloud-forming mineral produces an absorption feature at a unique and particle size-dependent wavelength, potentially allowing us to distinguish between cloud particle size and compositions directly. In Figure 7, we show thermal emission spectra and flux ratio plots for a range of cloud compositions, sizes, and crystalline structures. We show a few representative examples to demonstrate the trends we find when changing the composition, size, and crystalline structure of the cloud model.

3.3. The Amplitude Difference

To quantify the strength of the cloud absorption features, we calculate the amplitude difference. We compute the difference in the ratios of flux inside and outside a mineral feature to the same model with the wavelength dependence averaged out (gray cloud), as described in Section 3.2. We define the amplitude difference as

$$\text{amplitude difference} = \frac{F_{7\,\mu\rm m}}{F_{9-10\,\mu\rm m}} - \frac{F_{7\,\mu\rm m,gray}}{F_{9-10\,\mu\rm m,gray}}. \quad (8)$$

We choose 7 μm as an appropriate reference wavelength where there should be little cloud impact. Figure 8, shows a graphic representation of Equation (8), with an 1800 K, log $g = 5$, 1 μm particle enstatite model. We also show the same model, with the wavelength dependence taken out (gray). The bottom panel of Figure 8 shows the flux ratio inside and outside the wavelength windows of interest.

We calculate the amplitude difference for a range of particle sizes between 0.001 and 10 μm, shown in Figure 9, for enstatite, forsterite, and corundum. This figure summarizes the particle size dependence, where the Mie scattering effects occur only for particles smaller than a few microns.

3.4. Particle Size Dependence

We investigated the effect that particle size and composition have on thermal emission spectra. The top right panel in Figure 7 shows how different sized particles can significantly change the spectrum in the mid-IR. This figure shows the spectra and flux ratios for a range of particle sizes from 0.001–10 μm. We find that small particles 1 μm or less, produce the silicate feature, while particle sizes $\leqslant$0.1 μm produce the strongest feature. Once particles become larger than a few microns, the cloud becomes gray. Thus non-gray mineral features seen in observations are likely due to absorption from small particles.

3.5. Enstatite vs. Forsterite

Rainout equilibrium calculations predict that forsterite forms a more massive cloud deeper in a brown dwarf atmosphere, with a less massive enstatite cloud at higher altitudes. The top left panel in Figure 7 shows an amorphous 1 μm forsterite (red) and enstatite (blue) cloud model. Amorphous enstatite and forsterite have a distinct single absorption feature at ~9.35 μm

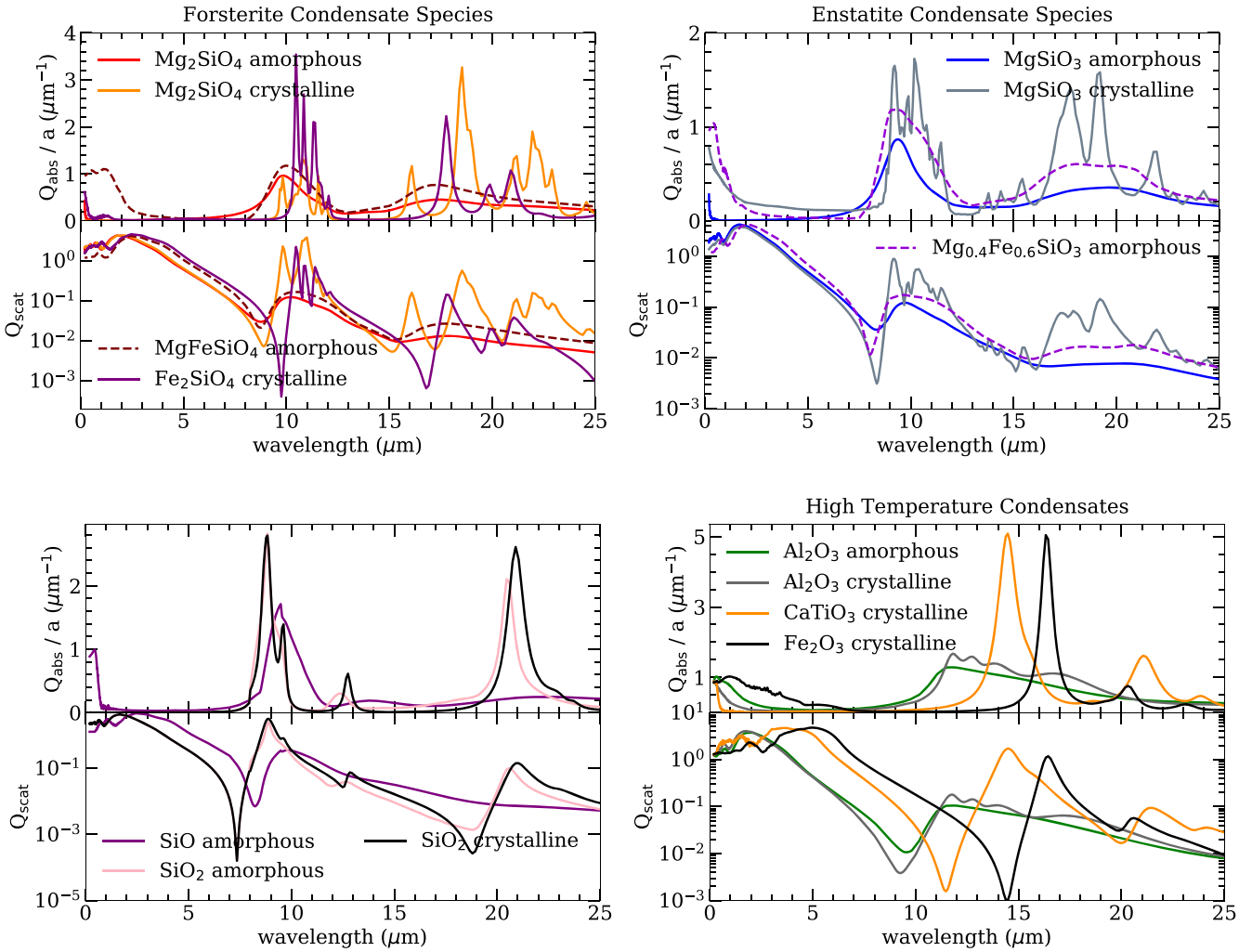

Figure 5. The absorption and scattering efficiencies for a range of condensates. The top panels show the forsterite and enstatite condensate species, where iron silicate variants are shown for both amorphous and crystalline structures. The bottom left panel shows silicon oxide species. The bottom right panel represents the high-temperature condensates that form in hot L dwarfs and super-hot Jupiters.

and ∼9.87 μm respectively. Since they are well separated in wavelength space, future mid-IR observations of brown dwarfs could distinguish between forsterite or enstatite.

3.6. Amorphous vs. Crystalline

It has been typical in the past to use optical properties of amorphous structures (AM01; Morley et al. 2012; Kitzmann & Heng 2018), thus most minerals investigated are that of amorphous glass or measured using the sol–gel method (Jäger et al. 2003). Amorphous and crystalline structures produce distinct spectral features. Crystalline structures produce deeper, narrower absorption features than amorphous structures, assuming the same particle size distributions and number density. We currently do not know the crystalline structure of cloud particles in brown dwarfs. However, it has been assumed that the silicate particles are in an amorphous state and that they may be the precursors to crystalline particles (Jäger et al. 2003). If a cloud particle rises and sinks in the atmosphere, annealing could happen to amorphous particles and cause them to crystallize. If this process occurs, mid-IR observations of brown dwarfs with small particles can reveal the crystalline structure.

3.7. Iron-rich Silicates

Standard brown dwarf cloudy models include iron droplets, but recent microphysical studies have shown that iron clouds do not readily form (Gao et al. 2021). Iron has a higher surface energy that creates a nucleation energy barrier preventing cloud formation (Gao et al. 2021). However, FeH disappears from the spectra of late L dwarfs (Kirkpatrick 2005) suggesting that iron is indeed removed from the gas phase. We explore the hypothesis that the iron, instead of condensing into droplets, is instead incorporated into silicate clouds. When iron is introduced to enstatite or forsterite they become pyroxene or olivine, respectively. We show model spectra for pyroxene compared to enstatite in the middle left panel of Figure 7 and demonstrate the trend we see for iron-rich silicate clouds. Increasing the iron content of either pyroxene or olivine pulls the absorption feature to bluer wavelengths.

3.8. Silicon Oxides and Refractory Clouds

The bottom two panels in Figure 7 show the silicon oxide species and high-temperature refractory cloud species for

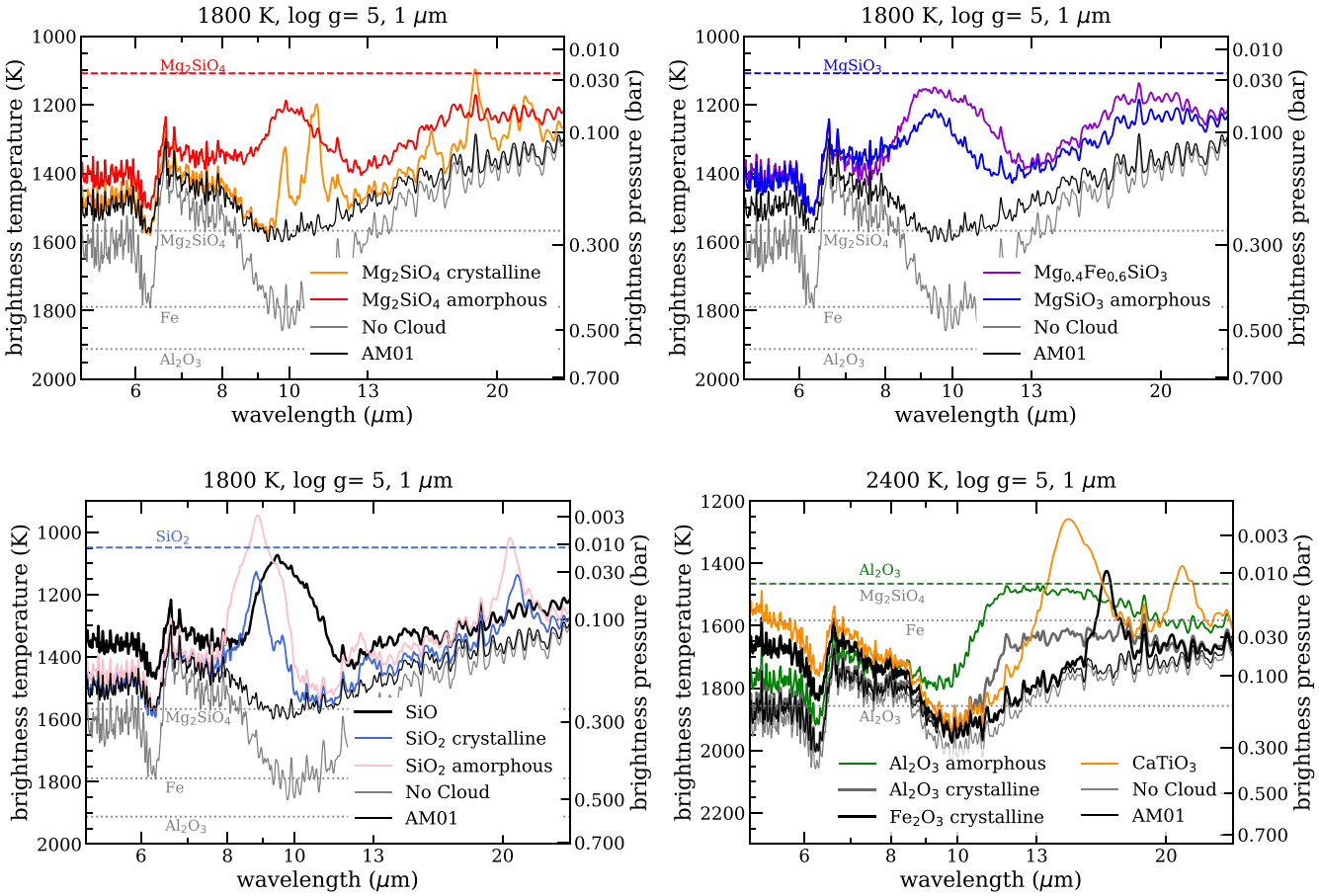

Figure 6. We show the brightness temperature for forsterite silicate species (top left), enstatite silicate species (top right), quartz species (bottom left), and high-temperature species (bottom right). The pressure along the pressure–temperature profile corresponding to each brightness temperature is shown on the right *y*-axis In each panel, we also show a cloud-free (gray) and an AM01, $f_{sed} = 2$ (black) model. The horizontal dashed gray lines represent the location of the standard AM01 clouds. The flux from each silicate or refractory features come from the top, cooler, part of the atmosphere (horizontal colored dashed lines). This is in contrast to the cloudless and AM01 models, where the flux in those regions come from the deeper, hotter part of the atmosphere.

1 μm particles. SiO uniquely absorbs at ~9.43 μm and crystalline and amorphous SiO_2 at ~8.83 and ~8.84 μm, respectively. The potential importance of these clouds is discussed further in Section 5.2.

Refractory clouds are expected to form in low-mass M dwarfs and super-hot Jupiters. Corundum is often included in standard brown dwarf cloud models (Ackerman & Marley 2001; Saumon & Marley 2008), but a variety of different refractory species could potentially condense. The initial Al-bearing and Ca-bearing condensates depend on the pressure and temperature of the atmosphere with different condensates being favored at different pressures (Lodders 2002; Wakeford et al. 2017). For example, in a solar composition gas perovskite ($CaTiO_3$) and corundum (Al_2O_3) are favored at low pressures, $Ca_4Ti_3O_{10}$ and hibonite ($CaAl_{12}O_{19}$) at intermediate pressures, and $Ca_3Ti_2O_7$ and grossite ($CaAl_4O_7$) at high pressures (Burrows & Sharp 1999; Lodders 2002; Wakeford et al. 2017). Corundum has a distinct absorption feature at ~11.42 μm for amorphous corundum and ~11.85 μm for crystalline corundum. Fe_2O_3 absorbs at ~14.3 μm and $CaTiO_3$ absorbs at ~16.35 μm. These high-temperature refractory clouds can potentially be seen in hot L dwarf spectra. However, these clouds do not form as abundantly as silicate condensates since the limiting gas species for each condensate is less abundant.

4. Matching Observations to Models

4.1. Fitting Spitzer IRS Data with Models

There are currently five brown dwarfs in the literature with a tentative silicate feature detection in their spectra using Spitzer IRS (listed in Table 2). Cushing et al. (2006) used Spitzer IRS to observe a sequence of low-mass objects and three objects show a tentative silicate feature. Looper et al. (2008) observed two more peculiar brown dwarfs that both show broad 8–10 μm absorption. One of these brown dwarfs, 2MASS J2148 +4003, will be observed in JWST cycle 1 under program ID: 2288 (PI: Joshua Lothringer, Co-PI: Jeff Valenti).

We find the best fitting model for each brown dwarf with a tentative Spitzer IRS silicate feature. We compare the model spectra to the data by computing the χ^2 between the data and model defined as

$$\chi^2 = \sum_{i=1}^{n} \left(\frac{f_i - F_{k,i}}{\sigma_i} \right)^2, \quad (9)$$

where n is the number of pixels in the data, f_i is the flux density of the data, $F_{k,i}$ is the flux density of the model, σ_i is the error for the observed flux density in the data. The model that corresponded to the smallest χ^2 was chosen as the best fitting model.

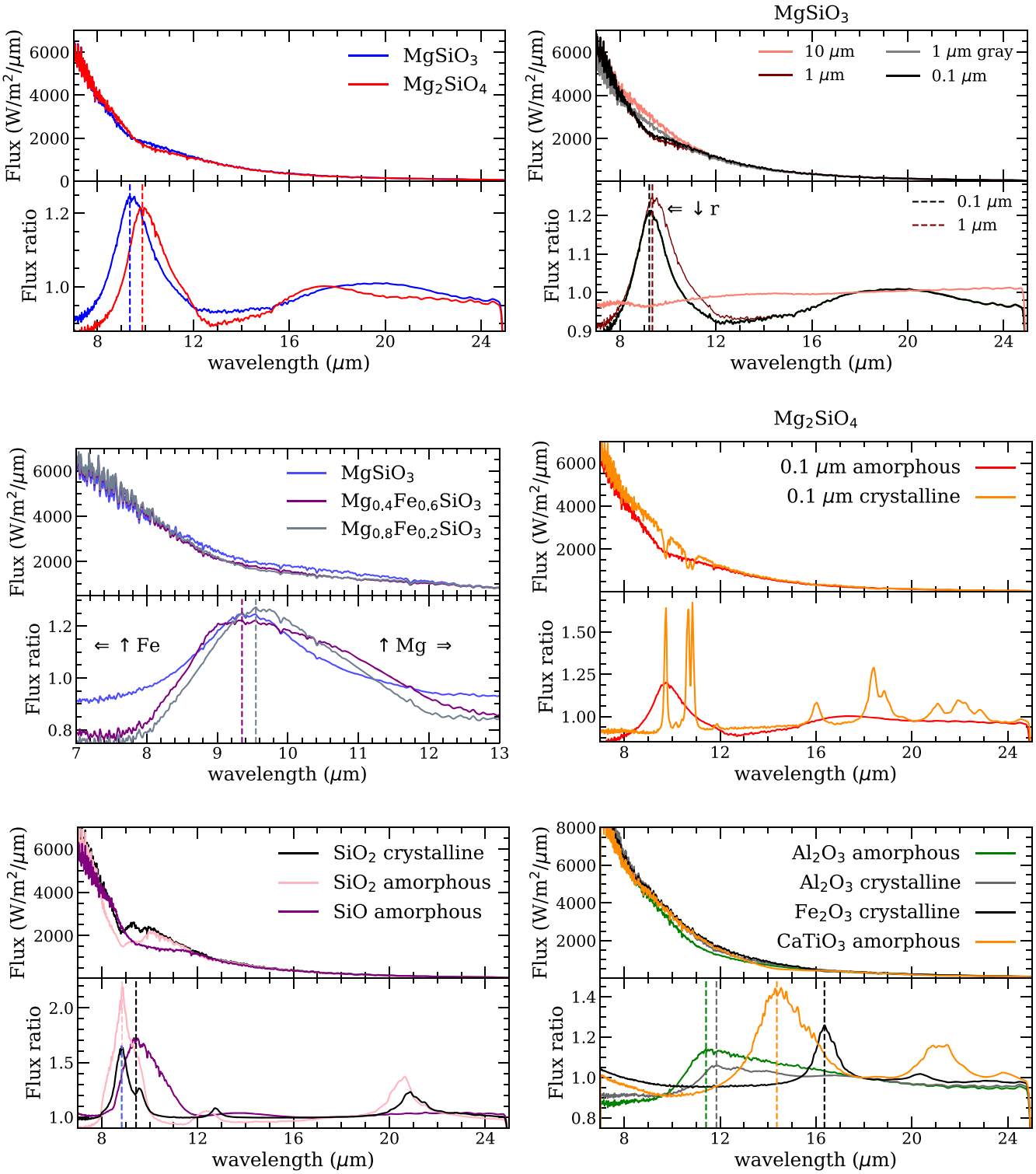

Figure 7. Thermal emission spectra and flux ratios for a range of particle sizes, compositions, and crystalline structures to demonstrate how the cloud mineral absorption feature changes. We use a 2400 K, log $g = 5$, 1 μm model spectrum for the high-temperature clouds (bottom right). All other panels use an 1800 K, log $g = 5$, 1 μm model spectrum.

The Spitzer/IRS spectra have $\lambda/\Delta\lambda \sim 90$ and each model spectrum is smoothed to this resolving power. In Table 3, we list the chi-squared value for all models fit to each brown dwarf. As a simple comparison between models, we also include whether the change in goodness of fit value is large enough to statistically reject models with worse fits than our best-fit model for each object. We highlight which models we can reject at the 3σlevel, assuming 184 degrees of freedom (189 data points in each IRS spectrum; five model parameters fit), though we note that no models provide perfect fits to the data. We note that this is a crude assessment using a coarse grid of models; future work could use more rigorous retrieval techniques to assess a more finely sampled set of model parameters as pioneered by Burningham et al. (2021) for

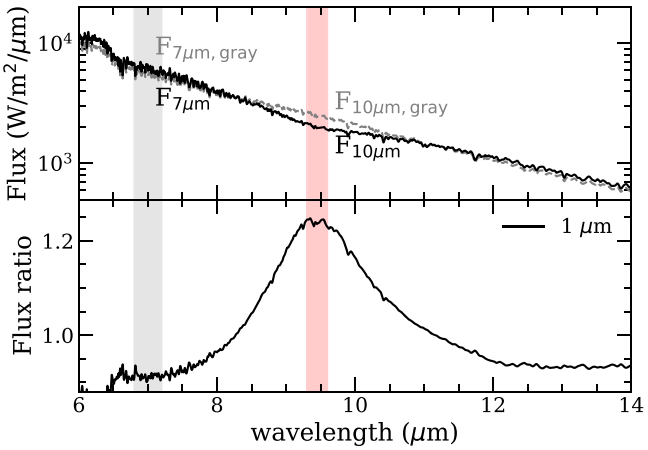

Figure 8. We demonstrate how we calculate the amplitude difference. The amplitude difference is simply the ratio of flux at two wavelengths: inside a mineral feature (shaded pink region) and outside (shaded gray region) where little variability is expected.

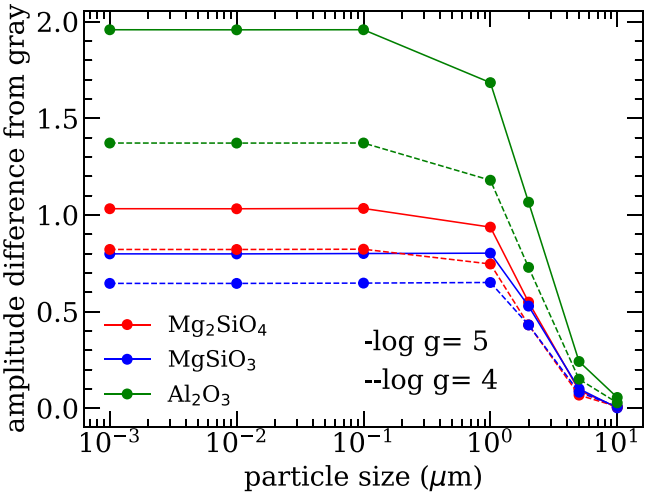

Figure 9. The amplitude difference of different particle sizes for forsterite, enstatite for an 1800 K model, and 2400 K for corundum. Particles that are 1 μm in size or less, produce a strong silicate feature. When particles are larger than a few microns, the Mie scattering features disappear and yield gray absorption.

cloudy L dwarfs. However, this simple and fast technique allows us to quickly assess how well different cloud species can fit the observed data.

2MASS J0036+1821 was best fit by an 1800 K, log $g = 5$, 0.1 μm enstatite cloud. We show the best fitting model in the top left panel of Figure 10 and an AM01 model with 1800 K, log $g = 5$, $f_{\rm sed} = 2$.

2MASS J1507-1627 was best fit by an 1700 K, log $g = 4$, 1 μm enstatite cloud. We show the best fitting model in the top right panel of Figure 10 and an AM01 model with 1700 K, log $g = 4$, $f_{\rm sed} = 2$.

2MASS J1821+1414 was best fit by an 1800 K, log $g = 5$, 1 μm enstatite cloud with a total cloud optical depth (somewhat higher than the standard $\tau_{\rm cloud} = 0.67$ set for the bulk of our models) $\tau_{\rm cloud} = 1$. We show the best fitting model in the middle left panel of Figure 10 and an AM01 model with 1800 K, log $g = 5$, $f_{\rm sed} = 2$.

2MASS J2148+4003 was best fit by an 1800 K, log $g = 5$, 1 μm enstatite cloud with a total cloud optical depth of $\tau_{\rm cloud} = 1$. We show the best fitting model in the middle right panel of Figure 10 and an AM01 model with 1800 K, log $g = 5$, $f_{\rm sed} = 2$. Looper et al. (2008) concluded that 2MASS J2148+4003 is possibly metal-rich, and the larger discrepancy between the model and data for this object may be attributed to the assumed solar composition atmosphere. Future studies should aim to compute higher-metallicity models to better capture the feature.

2MASS J2224-0158 was best fit by an 1800 K, log $g = 5$, 0.1 μm SiO cloud. We show the best fitting model in the bottom panel of Figure 10 and an AM01 model with 1800 K, log $g = 5$, $f_{\rm sed} = 2$. Similarly to J2148+4003, this brown dwarf may be metal-rich (Burningham et al. 2021).

Interestingly, we find that four of the five objects studied are better fit by an amorphous enstatite cloud than a forsterite cloud, which equilibrium rainout models predict to be more massive. This lends credence to the idea that because enstatite condenses at lower pressures, it may dominate spectroscopically.

4.2. Simulating Spectra with JWST/MIRI

We simulate spectroscopic observations of brown dwarfs with a tentative Spitzer silicate detection using the JWST. We use the publicly available JWST exposure time calculator (hereafter, JWST ETC) that calculates the signal-to-noise ratio (S/N) for all JWST observing modes (Pontoppidan et al. 2016) (https://jwst.etc.stsci.edu). We simulate spectroscopic observations with the MIRI instrument, in Medium-resolution spectroscopy (MRS) mode, which is capable of observing the full wavelength range of mineral features found in L dwarfs.

To determine the S/N for each object of interest we use the best fitting model from Section 4.1 as inputs to the JWST ETC. The model spectra give the flux as a function of wavelength at the surface of a brown dwarf. To obtain the flux at Earth, the best fitting model spectra must be multiplied by $(R/D)^2$, where R is the radius of the brown dwarf and D is the distance to the brown dwarf. We use the radius and distance for each brown dwarf from literature estimates (listed in Table 2).

We simulated data based on MIRI MRS with the first three channels. For each best fitting model spectrum, we simulate data using two exposure times for the first three channels in MIRI MRS: 837 and 2220 s. In Figure 11, we show a simulated JWST/MIRI Channel 2 spectrum for 2MASS J1507-1627 for a 837 s exposure. The area of the spectrum affected by cloud opacity from $MgSiO_3$ is shaded. This region of the spectrum is largely shaped by the gas opacity from H_2O but CH_4, SiO, CO_2, and H_2S can also be detectable in the MIRI bandpasses if present in the atmosphere. In each panel we also plot the error bar to scale in the upper right, before the channel names. The results presented in Section 4.1 and Burningham et al. (2021) demonstrate the Spitzer/IRS-like resolution (~90) and S/N (typically ~40 per resolution element) are adequately high for characterizing the broad features of silicate clouds. Observations with JWST will provide several advantages that we will briefly discuss here.

JWST/MIRI can achieve the same S/N per spectral element as Spitzer/IRS in roughly the same integration time, but with 30 times the spectral resolution. For example, in a 16 minute exposure on either JWST/MIRI (at 9.4 μm) or Spitzer/IRS yields an S/N of ~40 per spectral element. The increase in spectral resolution will potentially allow us to detect trace species like SiO, CH_4, CO_2, and H_2S at mid-infrared wavelengths (see Figure 11).

Table 2
Bright L Dwarfs with a Tentative Silicate Detection

Name	SpT	J	R ($R_\odot$)	D (pc)	P (hr)	A[3.6] (%)	A[4.5] (%)
2MASS J0036159+182110	L3.5	12.47	0.11	8.8 ± 0.1	2.7	0.47 ± 0.05	0.19 ± 0.04
2MASS J1507476-162738	L5	12.83	0.08	7.3 ± 0.03	2.5	0.53 ± 0.11	0.45 ± 0.09
2MASS J18212815+1414010	L4.5	13.43	0.09 (a)	9.3568 ± 0.022 (a)	4.2	0.54 ± 0.05	0.71 ± 0.14
2MASS J21481628+4003593	L6	14.15	0.10 (b)	7 ± 1 (c)	19	1.33 ± 0.07	1.03 ± 0.10
2MASS J2224438-015852	L4.5	14.07	0.12 (0.11–0.13)	11.5 ± 0.1	...	...	...

Note. Periods and amplitudes of variability for the 3.6 and 4.5 μm from Metchev et al. (2015). Radius and distance from Stephens et al. (2009) unless noted otherwise. 2MASS J2224438-015852 is not variable.
References. (a) Sebastian et al. (2021), (b) Vos et al. (2020), and (c) Faherty et al. (2009).

Binning JWST/MIRI observations to Spitzer/IRS-like resolutions, would enable us to characterize more distant objects. To achieve the same S/N ~ 40 in 16 minutes, we could observe objects ~5.5× further away. For context, the most distant mid-L dwarf with a silicate feature observed with Spitzer was 2MASS J2224438-015852 with a distance of 11.5 pc (Stephens et al. 2009). JWST will enable more observations of fainter and more distant brown dwarfs. We can potentially observe dozens more brown dwarfs at high S/N, allowing us to target interesting and more rare targets, such as very young brown dwarfs, or those with high or low metallicities, at a range of viewing geometries.

Lastly and perhaps obviously, Spitzer stopped operating cryogenically in 2009. Many brown dwarfs have been discovered since then, and many interesting fields of brown dwarf research have emerged or matured in that time, including studies of their variability (Metchev et al. 2015; Vos et al. 2019, 2020), obliquities (Bryan et al. 2020), and characteristics of youth (Vos et al. 2019, 2020). Directly studying the cloud optical properties will inform, and be informed by these fields.

4.3. Simulating Time-series Spectra with JWST/MIRI

Four brown dwarfs (2MASS J0036+1821, 2MASS J1507-1627, 2MASS J1821+1414, and 2MASS J2148+4003) with a tentative Spitzer silicate detections are also variable, suggesting that their atmospheres are inhomogeneous, potentially with patchy clouds (Bailer-Jones & Mundt 2001; Gelino et al. 2002; Radigan et al. 2014; Metchev et al. 2015). One way to determine the cause of brown dwarf variability is by studying the variability of the silicate feature itself.

Metchev et al. (2015) used the [3.6] and [4.5] Spitzer Infrared Array Camera (IRAC) channels to determine the amplitudes and periods of variability for field brown dwarfs (including the brown dwarfs in Section 4.1). We use the amplitudes at [3.6] and [4.5] and periods to guide simulations of variability in the mid-IR.

We simulate time-series observations of variable brown dwarfs with a tentative silicate detection on the JWST. We use the S/N estimates from Section 4.2 for the short exposure time (837 s) to simulate time-series observations with the MIRI instrument.

It is unknown which clouds are causing the brightness variations seen with Spitzer. There are two scenarios that we explore: one cloud changing and causing brightness variations or both clouds changing.

1. One cloud varying: In this case, the deep AM01 cloud is static while the ad hoc cloud in the upper layers of the atmosphere is undergoing weather.
2. Two clouds varying: In this case, both the deep AM01 cloud and the ad hoc cloud in the upper layers are undergoing weather and causing brightness variations.

To model one cloud varying, we calculate and sum the flux from two cloudy models. The first is an $f_{\rm sed} = 2$ AM01 cloud that becomes optically thick at 0.4 bar. The second includes an ad hoc cloud model above at 0.011 bar, as described in Section 2.2. We linearly combine the two cloudy models, varying the fraction of the AM01 and ad hoc cloud models. If one hemisphere is cloudier than the other, we will observe varying brightness as the two cloudy regions come in and out of view. We model the total flux from the two cloudy components as follows:

$$F_{\rm total} = f\ F_{\rm (ad\ hoc\ +\ AM)} + (1 - f)\ F_{\rm AM}, \quad (10)$$

where f is the fractional cloud coverage, $F_{\rm AM}$ is the flux from the AM01 cloud, and $F_{\rm (ad\ hoc\ +\ AM)}$ is equal to the flux from the ad hoc cloud.

To model two clouds varying, we assume both the ad hoc and AM01 cloud varies. To model both components as varying, we replace $F_{\rm AM}$, in Equation (10), with an alternative $F(\tau \times f_\tau)_{\rm ad\ hoc}$, where the cloud optical depth in each layer is multiplied by some fraction, f_τ. In this way, we are varying both the AM01 and the ad hoc cloud model. We use the fraction that can best match the observed Spitzer amplitudes of variability to simulate the variability in the mid-IR. We use a toy model sine curve to simulate the brightness variations we can expect from the mid-IR using the MIRI instrument on board JWST. This is a simplistic version of the modeling by Metchev et al. (2015) and non-sinusoidal variations in the amplitude and phase are to be expected. We show the light curves and fit from Metchev et al. (2015) in the top panels of Figures 12 and 13. To illustrate our simple toy model, we over plot the simulated [3.6] and [4.5] amplitudes of variability. This sine curve simply uses the period and amplitude in Table 2.

We now describe the steps to simulate the mid-IR variability.

1. Find the fraction, f, that best reproduces the observed Spitzer amplitudes of variability.
2. If possible find the fractions, f and f_τ, that can reproduce the observed Spitzer amplitudes of variability.
3. Using the fraction(s), we calculate the amplitudes of variability inside and outside the silicate feature.

We start by finding the correct fraction, f, that reproduces the observed amplitudes of variability in IRAC channels 1 and 2

Table 3
Goodness of Fit Values for all Model Fits for Each Brown Dwarf

Object	Condensate	T(K), log g, $r(\mu m)$, τ_{cloud}	χ^2	Reject?
J0036159+182110	$MgSiO_3$, amorphous	1800, 5, 1, 0.67	3078	N
J0036159+182110	$MgSiO_3$, amorphous	1800, 5,0.1, 0.67	3082	N
J0036159+182110	Mg_2SiO_4, amorphous	1800, 5, 0.1, 0.67	3305	Y
J0036159+182110	SiO_2, crystalline	1800, 5, 1, 0.2	3439	Y
J0036159+182110	SiO, amorphous	1800, 5, 0.1, 0.67	3538	Y
J0036159+182110	Mg_2SiO_4, amorphous	1800, 5, 1, 0.67	3525	Y
J0036159+182110	$MgSiO_3$, crystalline	1800, 5, 0.1, 0.2	3796	Y
J0036159+182110	SiO, amorphous	1800, 5, 1, 0.67	3833	Y
J0036159+182110	$MgSiO_3$, crystalline	1800, 5, 1, 0.2	3954	Y
J0036159+182110	Mg_2SiO_4, crystalline	1800, 5, 1, 0.2	4823	Y
J0036159+182110	Mg_2SiO_4, crystalline	1800, 5, 0.1, 0.2	4799	Y
J0036159+182110	SiO_2, crystalline	1800, 5,0.1, 0.2	4865	Y
J0036159+182110	SiO_2,amorphous	1800, 5,1, 0.67	4920	Y
J0036159+182110	SiO_2,amorphous	1800, 5,0.1, 0.67	6683	Y
J1507476-162738	$MgSiO_3$, amorphous	1700, 4, 1, 0.67	3518	N
J1507476-162738	$MgSiO_3$, amorphous	1700, 4, 0.1, 0.67	3609	Y
J1507476-162738	Mg_2SiO_4, amorphous	1700, 4, 0.1, 0.67	3903	Y
J1507476-162738	$MgSiO_3$, crystalline	1700, 4, 0.1, 0.2	3955	Y
J1507476-162738	$MgSiO_3$, crystalline	1700, 4, 1, 0.2	4050	Y
J1507476-162738	Mg_2SiO_4, amorphous	1700, 4, 1, 0.67	4000	Y
J1507476-162738	SiO_2, crystalline	1700, 4, 1, 0.2	4344	Y
J1507476-162738	SiO, amorphous	1700, 4, 0.1, 0.67	4838	Y
J1507476-162738	SiO, amorphous	1700, 4, 1, 0.67	4908	Y
J1507476-162738	Mg_2SiO_4, crystalline	1700, 4, 1, 0.2	5138	Y
J1507476-162738	Mg_2SiO_4, crystalline	1700, 4, 0.1, 0.2	5222	Y
J1507476-162738	SiO_2, crystalline	1700, 4, 0.1, 0.2	6170	Y
J1507476-162738	SiO_2, amorphous	1700, 4, 1, 0.67	7376	Y
J1507476-162738	SiO_2, amorphous	1700, 4, 0.1, 0.67	9236	Y
J18212815+1414010	$MgSiO_3$, amorphous	1800, 5, 1, 1	2999	N
J18212815+1414010	$MgSiO_3$, amorphous	1800, 5, 1, 0.67,	3063	Y
J18212815+1414010	$MgSiO_3$, amorphous	1800, 5, 0.1, 0.67	3315	Y
J18212815+1414010	SiO, amorphous	1800, 5, 0.1, 0.4	3329	Y
J18212815+1414010	SiO, amorphous	1800, 5, 0.1, 0.3	3318	Y
J18212815+1414010	$MgSiO_3$, amorphous	1800, 5, 0.1, 1	3836	Y
J18212815+1414010	SiO_2, crystalline	1800, 5, 1, 0.2	3554	Y
J18212815+1414010	SiO, amorphous	1800, 5, 1, 0.4	3661	Y
J18212815+1414010	Mg_2SiO_4, amorphous	1800, 5, 0.1, 0.67	3962	Y
J18212815+1414010	SiO, amorphous	1800, 5, 1, 0.3	3719	Y
J18212815+1414010	SiO, amorphous	1800, 5, 0.1, 0.4	4133	Y
J18212815+1414010	Mg_2SiO_4, amorphous	1800, 5, 1, 0.67	4018	Y
J18212815+1414010	$MgSiO_3$, crystalline	1800, 5, 0.1, 0.2	4168	Y
J18212815+1414010	SiO, amorphous	1800, 5, 1, 0.67	4044	Y
J18212815+1414010	$MgSiO_3$, crystalline	1800, 5, 1, 0.2	4478	Y
J18212815+1414010	SiO_2, crystalline	1800, 5, 0.1, 0.2	5645	Y
J18212815+1414010	SiO_2, amorphous	1800, 5, 1, 0.67	5831	Y
J18212815+1414010	Mg_2SiO_4, crystalline	1800, 5, 0.1, 0.2	6149	Y
J18212815+1414010	Mg_2SiO_4, crystalline	1800, 5, 1, 0.2	6316	Y
J18212815+1414010	Mg_2SiO_4, amorphous	1800, 5, 0.1, 0.67	8150	Y
J21481628+4003593	$MgSiO_3$, amorphous	1800, 5, 0.1, 1	6000	N
J21481628+4003593	$MgSiO_3$, amorphous	1800, 5, 1, 1	6067	Y
J21481628+4003593	SiO, amorphous	1800, 5, 0.1, 0.67	6348	Y
J21481628+4003593	$MgSiO_3$, amorphous	1800, 5, 0.1, 0.67	7050	Y
J21481628+4003593	SiO, amorphous	1800, 5, 0.1, 0.4	7099	Y
J21481628+4003593	$MgSiO_3$, amorphous	1800, 5, 0.1, 0.67	7536	Y
J21481628+4003593	SiO, amorphous	1800, 5, 0.1, 0.3	8178	Y
J21481628+4003593	SiO_2, crystalline	1800, 5, 0.1, 0.2	8376	Y
J21481628+4003593	SiO_2, amorphous	1800, 5, 0.1, 0.67	8158	Y
J21481628+4003593	Mg_2SiO_4, amorphous	1800, 5, 0.1, 0.67	8881	Y
J21481628+4003593	SiO, amorphous	1800, 5, 0.1, 0.67	9181	Y
J21481628+4003593	SiO, amorphous	1800, 5, 1, 0.4	9551	Y
J21481628+4003593	SiO, amorphous	1800, 5, 1, 0.3	10314	Y
J21481628+4003593	Mg_2SiO_4, amorphous	1800, 5, 1, 0.67	10634	Y

Table 3
(Continued)

Object	Condensate	T(K), log g, r(μm), $\tau_{\rm cloud}$	χ^2	Reject?
J21481628+4003593	$MgSiO_3$, crystalline	1800, 5, 0.1, 0.2	11410	Y
J21481628+4003593	$MgSiO_3$, crystalline	1800, 5, 1, 0.2	12802	Y
J21481628+4003593	SiO_2, crystalline	1800, 5, 0.1, 0.2	13727	Y
J21481628+4003593	SiO_2, amorphous	1800, 5, 0.1, 0.67	13873	Y
J21481628+4003593	Mg_2SiO_4, crystalline	1800, 5, 0.1, 0.2	17863	Y
J21481628+4003593	Mg_2SiO_4, crystalline	1800, 5, 1, 0.2	18757	Y
J2224438-015852	SiO, amorphous	1800, 5, 0.1, 0.67	1759	N
J2224438-015852	$MgSiO_3$, amorphous	1800, 5, 0.1, 0.67	2002	Y
J2224438-015852	Mg_2SiO_4, amorphous	1800, 5, 0.1, 0.67	2139	Y
J2224438-015852	$MgSiO_3$, amorphous	1800, 5, 1, 0.67	2491	Y
J2224438-015852	SiO_2, crystalline	1800, 5, 1, 0.2	2253	Y
J2224438-015852	SiO_2, amorphous	1800, 5, 1, 0.67	2326	Y
J2224438-015852	SiO, amorphous	1800, 5, 1, 0.67	2723	Y
J2224438-015852	Mg_2SiO_4, amorphous	1800, 5, 0.1, 0.67	2736	Y
J2224438-015852	$MgSiO_3$, crystalline	1800, 5, 1, 0.2	3258	Y
J2224438-015852	$MgSiO_3$, crystalline	1800, 5, 0.1, 0.2	3356	Y
J2224438-015852	SiO_2, crystalline	1800, 5, 0.1, 0.2	3179	Y
J2224438-015852	SiO_2, amorphous	1800, 5, 0.1, 0.67	2957	Y
J2224438-015852	Mg_2SiO_4, crystalline	1800, 5, 0.1, 0.2	3862	Y
J2224438-015852	Mg_2SiO_4, crystalline	1800, 5, 1, 0.2	4050	Y

Note. Chi-square values for each model.

from Metchev et al. (2015). To do this we use the best fitting model from Section 4.1 and a standard $f_{\rm sed} = 2$, AM01 cloud model. Using Equation (10), we combine the flux from the cloudy models using a range of fractions f, 0.1–0.5 in steps of 0.005. We then integrate the flux in the first two IRAC filter channels [3.6] and [4.5] and compute the amplitudes in the two channels. We then choose the fraction that yielded the smallest χ^2 to the observed Spitzer amplitudes of variability and associated errors listed in Table 2. In the case where both clouds are varying, we chose the combination of f and f_τ that yielded the smallest χ^2. We explored a range of f_τ's, 0.1–0.9 in steps of 0.1.

Next, we describe the steps we use to simulate the variability in the mid-IR. We start by modeling the clouds as varying using the fraction that best reproduces the observed Spitzer amplitudes of variability. Using this best fraction, we calculate the amplitudes of variability from 9–10 μm (A [9–10 μm]) and from 6.5–7.5 μm (A [7 μm]). We then attempt the same process, but by varying both clouds. We calculate the A [3.6 μm] and A [4.5 μm] for each combination of fractions f (0.1–0.5 in steps of 0.005) and f_τ (0.1–0.9 in steps of 0.1). Using the fractions, f and f_τ, that gives the smallest χ^2, we calculate A [7 μm] and A [9–10 μm]. We should expect that the variability inside the silicate feature (9–10 μm) to be larger than the variability at a reference wavelength, which we choose as 7 μm.

4.3.1. 2MASS J0036+1821

We were able to reproduce the observed amplitudes of variability for this object by varying one or two clouds. The fraction $f = 0.455$ gives A [3.6 μm] = 0.52% and A [4.5 μm] = 0.16%. The predicted variability in the mid-IR is shown in the top panel of Figure 12. The variability inside the silicate feature is ∼4 times the variability outside the feature.

The combination of fractions $f = 0.28$ and $f_\tau = 0.6$ gives A [3.6 μm] = 0.46% and A [4.5 μm] = 0.20%. The predicted variability in the mid-IR is shown in the bottom panel of Figure 12. Although the variability is larger in the silicate feature, the difference in amplitudes at each wavelength decreases.

4.3.2. 2MASS J1507-1627

We were able to reproduce the observed amplitudes of variability for this object only by varying the ad hoc cloud alone. The fraction $f = 0.26$ gives A [3.6 μm] = 0.51% and A [4.5 μm] = 0.47%. We show the predicted mid-IR variability in the bottom panel of Figure 13. The variability inside the silicate feature is ∼2 times the variability outside the feature.

4.3.3. 2MASS J1821+1414

We were able to reproduce the observed amplitudes of variability for this object only by varying the ad hoc cloud alone. The fraction $f = 0.37$ gives A [3.6 μm] = 0.62% and A [4.5 μm] = 0.56%. We show the predicted mid-IR variability in the bottom panel of Figure 14. The variability inside the silicate feature is ∼11 times the variability outside the feature.

4.3.4. 2MASS J2148+4003

We were able to reproduce the observed amplitudes of variability for this object only by varying the ad hoc cloud alone. The fraction $f = 0.235$ gives A [3.6 μm] = 1.25% and A [4.5 μm] = 1.14%. We show the predicted mid-IR variability in the bottom panel of Figure 15. The variability inside the silicate feature is ∼11 times the variability outside the feature.

5. Discussion

5.1. Small Particles in Cloud Models

Our results show that small particles at low pressures are needed to produce the silicate feature. Simple advective-diffusive balance cloud models (e.g., AM01) typically have

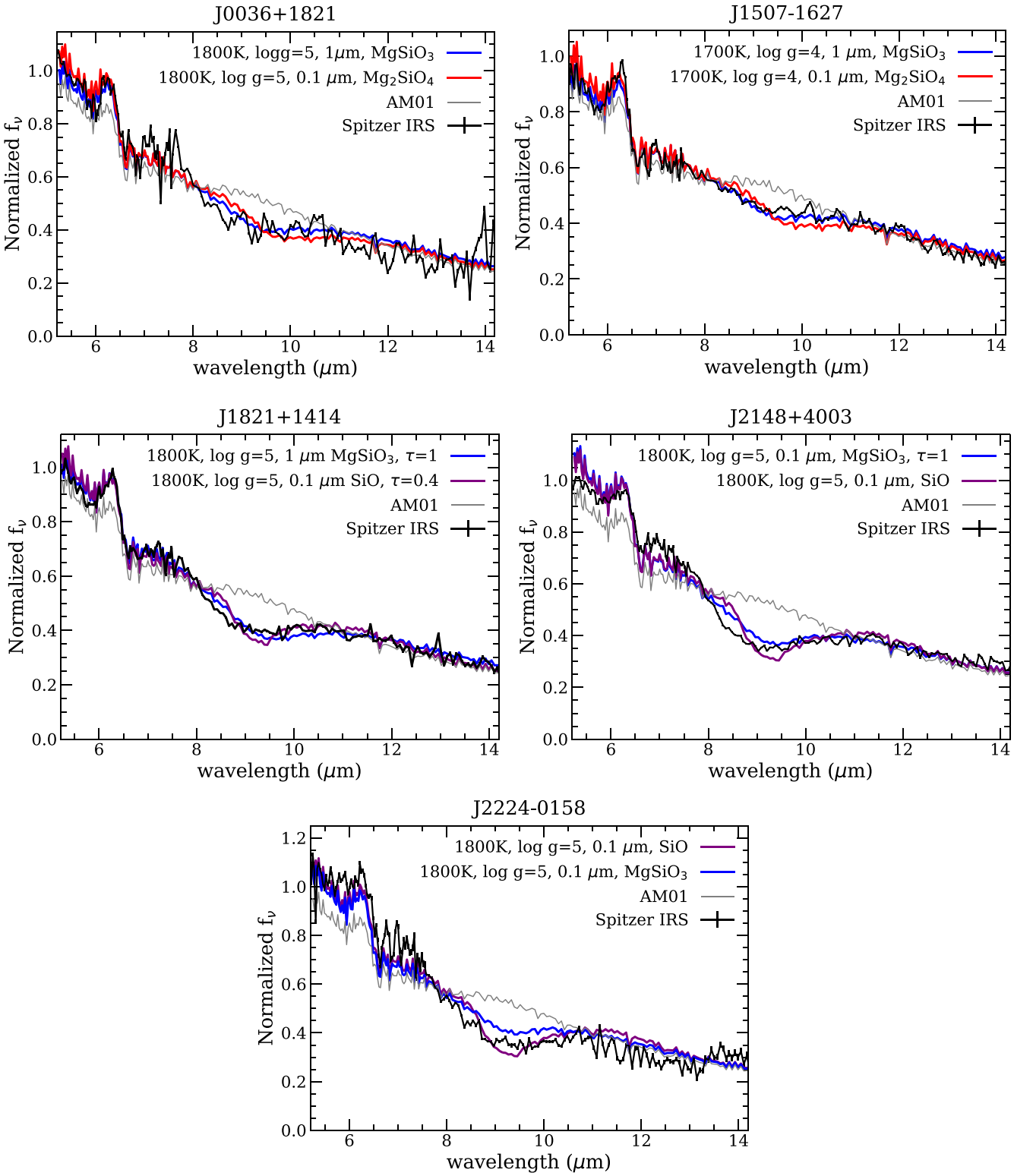

Figure 10. Brown dwarf observations taken with the Spitzer IRS that tentatively show the silicate feature (Cushing et al. 2006; Looper et al. 2008) at $\lambda/\Delta\lambda \sim 90$. The gray line represents a standard AM01 cloud model for an $f_{sed} = 2$ with the temperature and surface of the corresponding best fitting model. The models are smoothed to the resolving power of the Spitzer IRS spectra. The black line represents the Spitzer IRS data with the observed errors. We also show the second best fitting model and list the χ^2 goodness of fit values in Table 3. Each cloud type is represented by a different color: enstatite in blue, forsterite in red, and SiO in purple.

larger particle sizes (e.g., $r = 10$–100 μm) and higher pressures ($P = 0.1$–1 bar) for typical ~1800 K L dwarfs. At least a subset of brown dwarfs have small particles in their clouds that remain uncaptured by these models.

Our results agree with Hiranaka et al. (2016), who showed that small particles above the main cloud deck could successfully reproduce the NIR colors of red brown dwarfs. Microphysical models do produce substantially small particles.

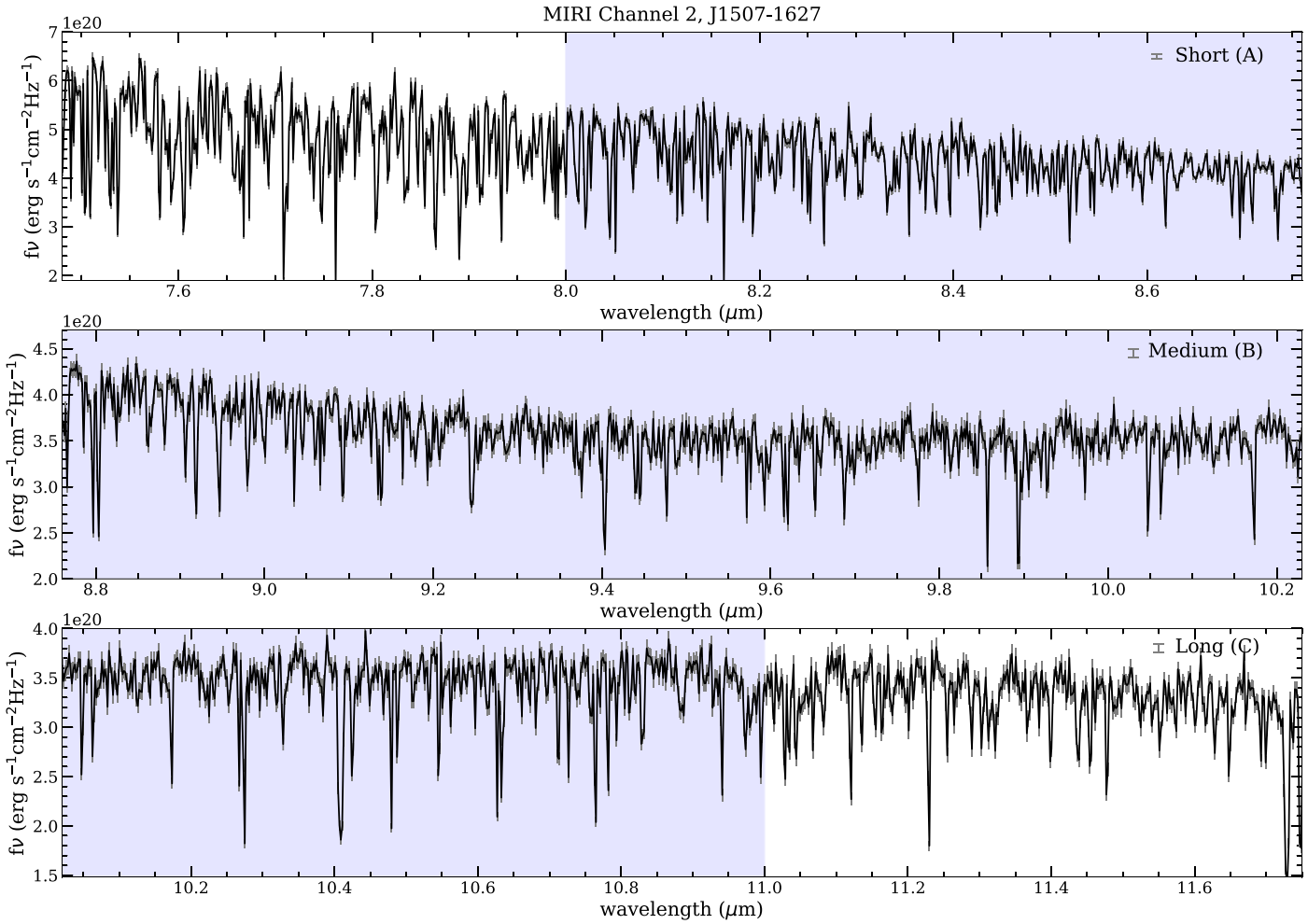

Figure 11. JWST/MIRI Channel 2 spectra for 2MASS J1507-1627 for a 837 s exposure. The error bars are plotted in gray and we show an example error bar to scale in the upper right, before the channel names. The area of the spectrum affected by cloud opacity from $MgSiO_3$ is shaded and this region of the spectrum is largely shaped by gas opacity from H_2O.

For example, using the CARMA model, Powell et al. (2018) found small particles can significantly dominate the cloud opacity when taking into account the full size particle distributions. In the era of JWST, forward models and retrievals alike should be modified such that they can capture absorption from these small particles.

Current retrievals of brown dwarfs often simplistically parameterize clouds by approximating the cloud as gray, power law, or not including clouds at all (Line et al. 2015; Burningham et al. 2017). Our work suggests that future retrieval work for brown dwarfs could retrieve information about particle size, composition, and crystalline structure (see Burningham et al. 2021).

5.2. Determining the Physics of Cloud Condensation

Determining the cloud condensation sequence in brown dwarfs will allow us to provide constraints on derived abundances. Clouds remove limited gaseous species (e.g., oxygen) from their atmospheres. The dominant silicate species for L dwarfs will result in more or less oxygen remaining in cooler objects; if most silicates form as $MgSiO_3$, 3 oxygen atoms are removed per magnesium atom, whereas if they form as Mg_2SiO_4, 2 oxygen atoms are removed per magnesium atom. This impacts our measurements of both brown dwarfs and exoplanets for which we measure molecular abundances and C/O ratios. JWST/MIRI observations can reveal the dominant silicate cloud mineral. One possibility is that brown dwarfs will follow rainout equilibrium calculations and condense predominantly forsterite. Another possibility is that enstatite will dominate the spectrum since it may be at higher altitudes than forsterite. Similarly, the cloud absorption features observed will shed light on the crystalline structure. Our results from fitting Spitzer IRS spectra suggest that many of these objects may have predominately enstatite clouds with optical constants consistent with amorphous, Mg-rich crystal structures.

We find that 2MASS J2224-0158 is marginally better fit by an SiO cloud than either $MgSiO_3$ or Mg_2SiO_4. Here, we discuss the plausibility of this cloud species. SiO is the most abundant silicon gas species over a wide range of pressures and temperatures (Visscher et al. 2010). SiO abundances can control silicate cloud formation (e.g., Helling & Woitke 2006; Powell et al. 2018). However, many cloud models do not include direct SiO condensation. Helling et al. (2006) proposed SiO_2 as the possible condensate responsible for the broad absorption seen in three brown dwarfs from Cushing et al. (2006) using grain chemistry models. Furthermore, Helling et al. (2008b) found that some SiO can form in the uppermost layers, broadly consistent with our fitted model containing SiO in the upper layers of the atmosphere. We suggest that future

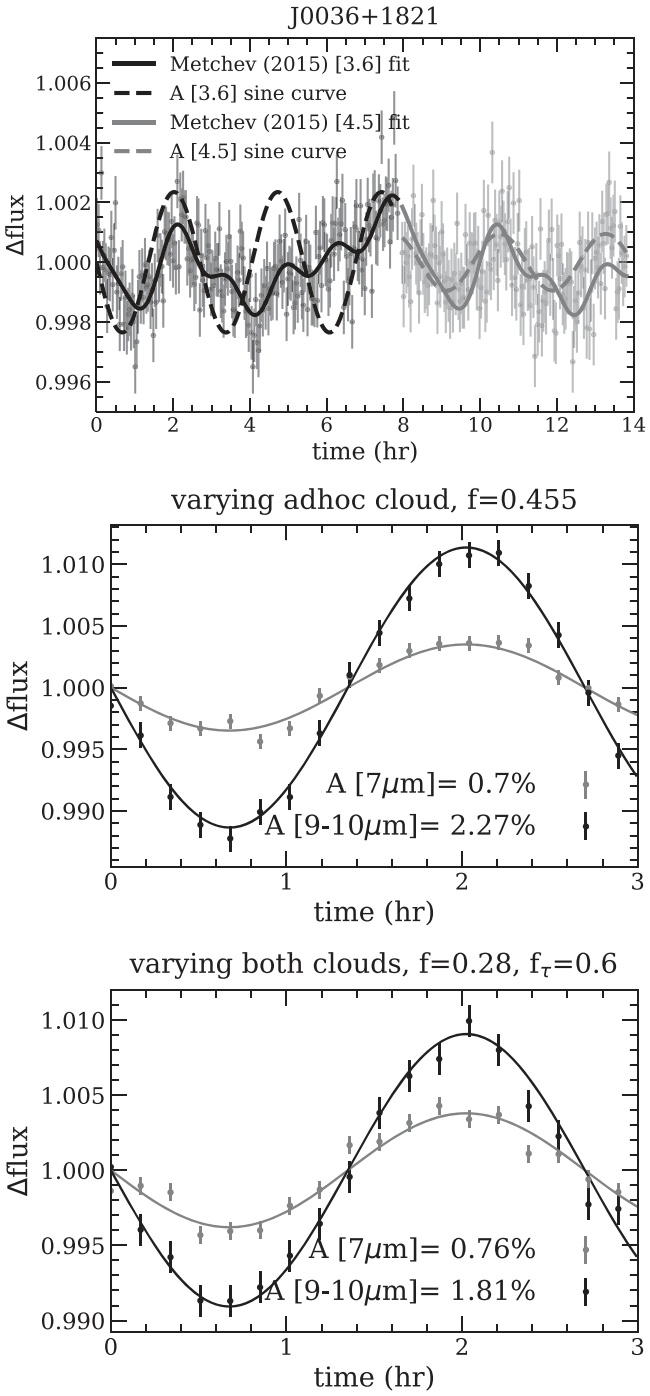

Figure 12. Spitzer light curves from Metchev et al. (2015) for J0036+1821 (top). The IRAC [3.6] points are in black and IRAC [4.5] points are in gray with the corresponding fit. We also show in black (dashed) and gray (dashed), the simplistic sine curve model that use the period and amplitude in Table 2. We show the predicted mid-IR variability for J0036+1821 by varying the ad hoc cloud (middle) and by varying both clouds (bottom).

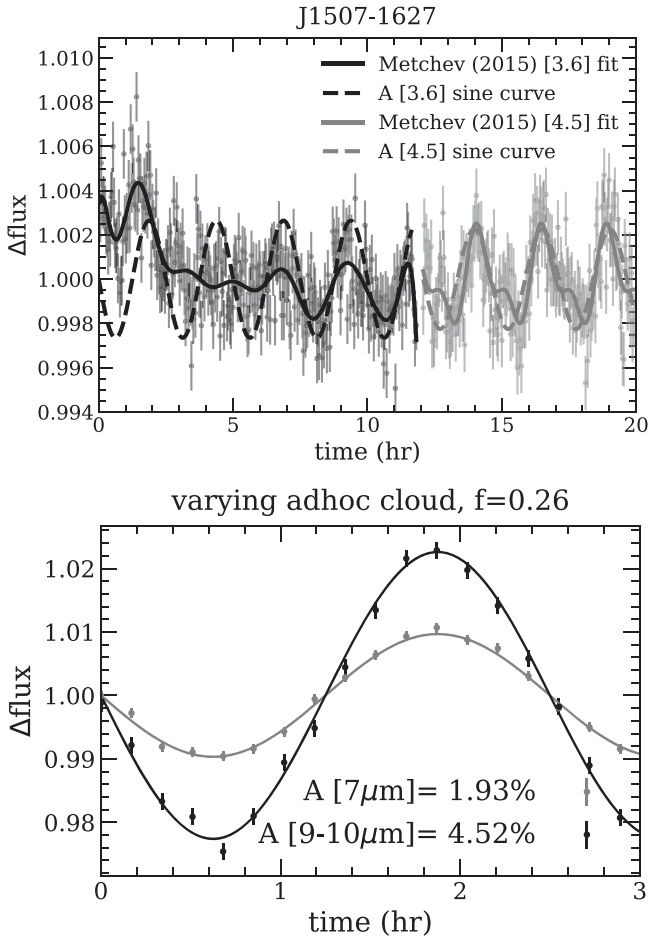

Figure 13. Spitzer light curves from Metchev et al. (2015) for J1507-1627 (top). The IRAC [3.6] points are in black and IRAC [4.5] points are in gray with the corresponding fit. We also show in black (dashed) and gray (dashed), the simplistic sine curve model that use the period and amplitude in Table 2. We show the predicted mid-IR variability for J1507-1627 by varying the ad hoc cloud (bottom).

cloud modeling remains open to this possibility. Recently, Burningham et al. (2021) used the *Brewster* retrieval framework to fit the 1–15 μm Spitzer/IRS spectrum of 2MASS J2224-0158. They found that the data was best fit with enstatite and quartz slabs at low pressures and an Fe cloud deck deeper in the atmosphere. This is similar to our findings, where our best fitting model is an SiO cloud at low pressures and an Fe cloud at higher pressures (+Al_2O_3 and Mg_2SiO_4, see Figure 10). Additionally 2MASS J2224-0158 was inferred to have a high-metallicity atmosphere from the estimated Mg/Si and C/O ratios (Burningham et al. 2021). This is similar to 2MASS J2148+4003, whose goodness of fit values were significantly worse for 2MASS J2148+4003 than for any other object (see Table 3). Future studies should aim to model atmospheres over a wide range of metallicities. During Spitzer's Cold mission that ended in 2009, it observed 106 L/T dwarfs using Spitzer/IRS. Since the end of its cold mission, hundreds of brown dwarfs have been discovered. Furthermore, brown dwarfs have since been discovered to be variable on the few percent level. JWST will enable follow-up spectroscopic observations of faint brown dwarfs to continue making strides in understanding the nature of these objects. Future JWST programs that aim to observe a wide range of cloudy brown dwarfs will enable more observations of the silicate feature. Additionally, the larger spectral range of MIRI will enable discoveries of other mineral features at longer wavelengths (e.g., Al_2O_3 at 12 μm, $CaTiO_3$ at 16 μm).

5.3. Lofting of Particles by Vertical Mixing

While silicates condense at pressures ~0.1–0.2 bar in typical L dwarfs, to match the silicate feature they must be lofted to

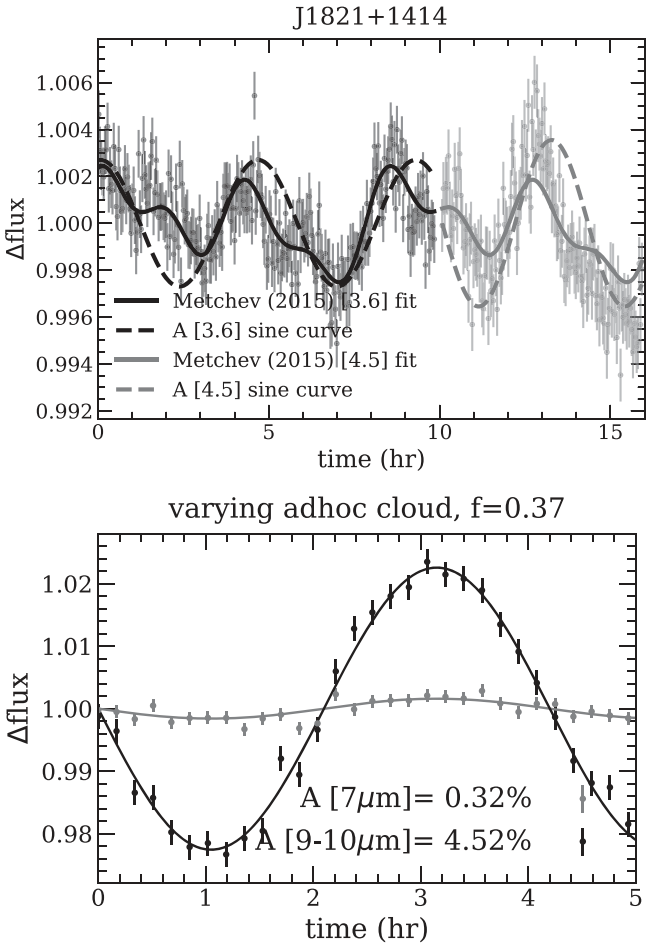

Figure 14. Same as Figure 13 for J1821+1414.

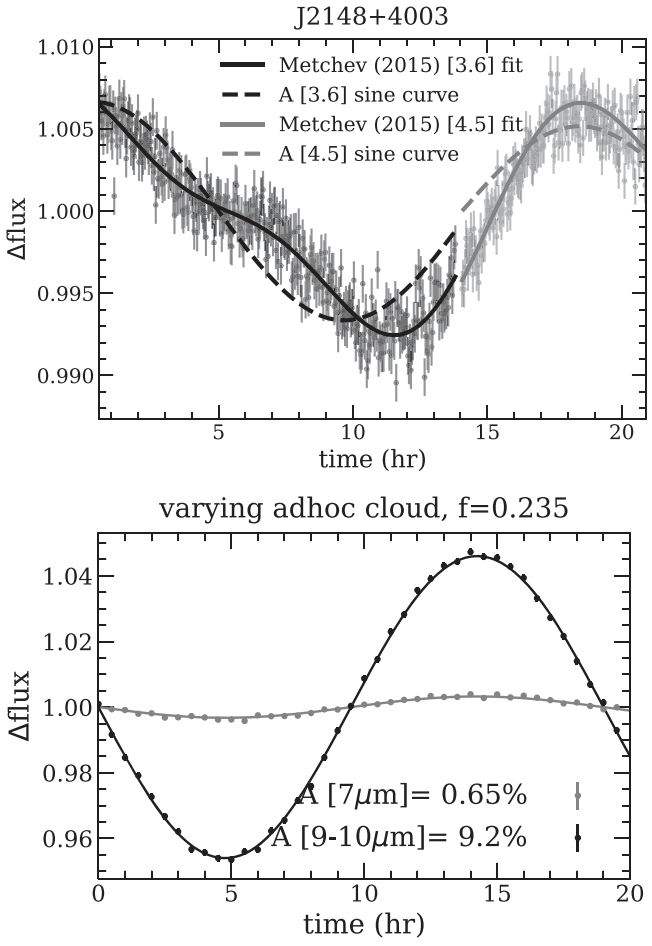

Figure 15. Same as Figure 13 for J2148+4003.

~0.01 bars. We can estimate how long the particles will stay lofted by comparing vertical mixing and settling timescales.

We compare the lofting timescale for a given vertical eddy diffusion coefficient, K_{zz}, to the falling timescale. K_{zz} is calculated within the atmosphere model, assuming mixing length theory in the convective region. Figure 16 shows the time for a particle to fall one pressure scale height defined as, $H/v_{\rm fall}$, where H is the scale height, and $v_{\rm fall}$ is the particle falling velocity. We follow the appendix of AM01 to calculate the falling velocities assuming viscous flow. We find that the lofting timescale is shorter than the falling timescale for particles less than 1 μm, indicating that small particles could stay lofted high in the atmosphere with vigorous enough mixing.

5.4. Temperature-dependent Optical Constants

The majority of optical constants used for silicates are measured at room temperature. This is much lower than the temperatures of L dwarfs. We explored the differences in the thermal emission spectra for temperature-dependent optical properties for orthoenstatite ($Mg_{0.92}Fe_{0.09}SiO_3$) at 10, 300, and 928 K (Zeidler et al. 2015). The crystalline orthoenstatite was measured on three crystallographic axes and we combine the information from each axis as described in Section 2.3 and shown in Figure 17. Using an 1800 K, log $g = 5$ model with 1 μm particles we computed model thermal emission spectra for the temperature-dependent optical constants shown in

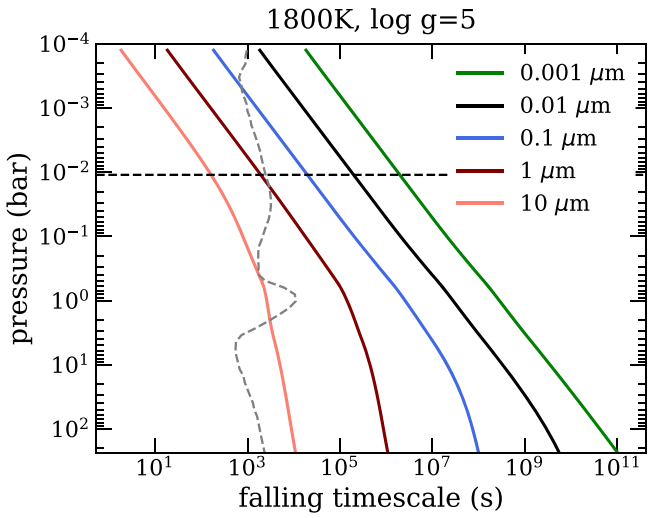

Figure 16. Falling timescales for cloud particles for an 1800 K, log $g = 5$ model. We show the $\tau \sim 1$ pressure where the ad hoc cloud is placed (dashed black). The solid lines show the time it takes a particle to fall one pressure scale height for a range of particle sizes. The gray dashed line shows the falling timescale for the K_{zz} of each pressure layer.

Figure 18. We find that as the temperature increases the absorption features become broader and shallower. Additionally, the peak in the absorption feature moves redder $\Delta\lambda \approx 0.13$ μm.

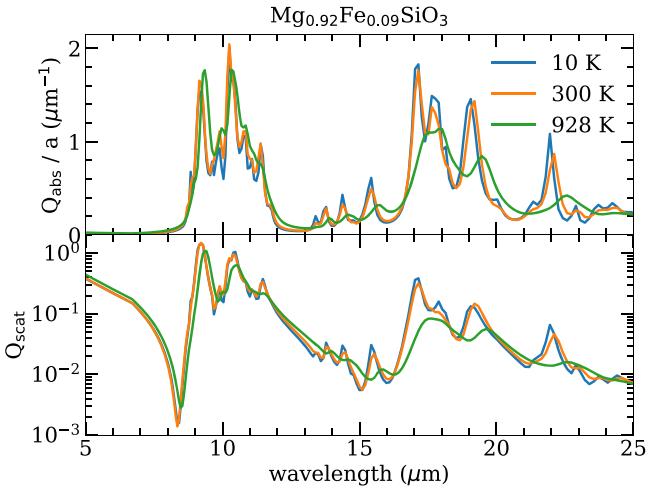

Figure 17. The absorption and scattering efficiencies for temperature-dependent orthoenstatite ($Mg_{0.92}Fe_{0.09}SiO_3$) at 10, 300, and 928 K for 1 μm particles.

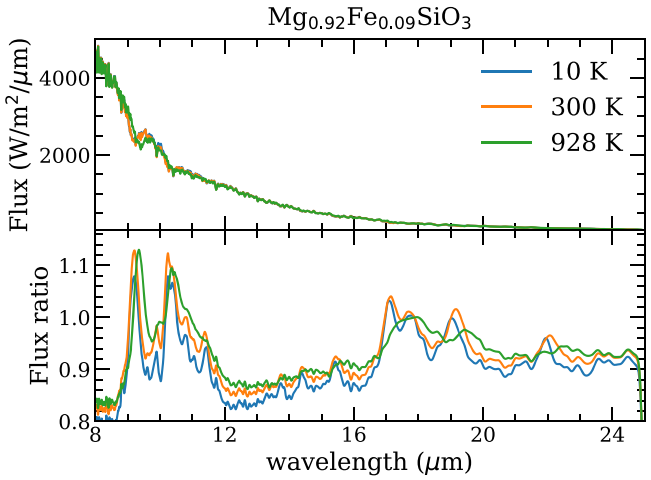

Figure 18. Thermal emission spectra and flux ratios for temperature-dependent optical constants of orthoenstatite ($Mg_{0.92}Fe_{0.09}SiO_3$) at 10, 300, and 928 K. We use an 1800 K, log $g = 5$ atmosphere with 1 μm particles.

Temperature-dependent optical constants were not available for other materials studied here. Future studies of optical constants should aim to explore a range of optical constants closer to the astrophysical environments being studied.

5.5. Application to Directly Imaged Exoplanets

Observations and models of brown dwarfs provide a testbed to study directly imaged exoplanet atmospheres. Some directly imaged planets are in the same temperature range as brown dwarfs and thus may show the same cloud mineral features in their thermal emission spectrum.

Vos et al. (2019) found that young brown dwarfs are more likely to be variable by studying the NIR variability in the J band. Recently, Spitzer IRAC observations of young low-gravity brown dwarfs revealed an increase in variability amplitudes for late L dwarfs at 4.5 μm (Vos et al. 2020). JWST/MIRI observations of young brown dwarfs could reveal the silicate feature in the mid-IR (Danielski et al. 2018; Brande et al. 2020). Some of these observations may also be possible for directly imaged exoplanets with JWST. Understanding the atmospheres of these young brown dwarfs is imperative for advancing knowledge of directly imaged exoplanets.

6. Conclusion

We presented models for silicate and refractory clouds in warm brown dwarf atmospheres. These models include small particles in the upper layers of the atmosphere and have unique absorption features in the mid-IR.

JWST/MIRI will potentially allow us to determine the cloud compositions, particle sizes, and mineral structures for warm brown dwarfs that have a sufficiently strong silicate feature. Soon, 2MASS J2148+4003 will be observed with JWST/MIRI in cycle 1 under program ID: 2288 (PI: Joshua Lothringer, Co-PI: Jeff Valenti), and its spectrum will shed light on the nature of clouds in this brown dwarf. Time-series spectroscopy would allow us to establish patchy clouds as the cause for brightness variations seen in brown dwarfs and provide information about the inhomogeneity of different cloud layers. These measurements will allow us to empirically establish the condensation sequence for substellar atmospheres and test models of cloud physics and chemistry, with implications for studies of cooler brown dwarfs and exoplanets.

We thank the reviewer for their thoughtful and helpful comments, which have improved the manuscript. This material is based upon work supported by the National Science Foundation Graduate Research Fellowship Program under grant No. DGE-1610403. Any opinions, findings, and conclusions, or recommendations expressed in this material are those of the authors and do not necessarily reflect the views of the National Science Foundation. J.L. and C.V.M. acknowledge the National Science Foundation, which supported the work presented here under grant No. 1910969.

This work benefited from the 2019 Exoplanet Summer Program in the Other Worlds Laboratory (OWL) at the University of California, Santa Cruz, a program funded by the Heising-Simons Foundation. We thank Stanimir Metchev for providing the reduced Spitzer light curves. J.L. thanks Brittany Miles for insights using the JWST ETC for brown dwarf observations. J.L. also thanks Jeremy Ritter for help with python data frames and useful UNIX code used to create plots made in this paper.

Software: astropy (Astropy Collaboration et al. 2013), spectres (Carnall 2017).

ORCID iDs

Jessica L. Luna https://orcid.org/0000-0003-2152-9248
Caroline V. Morley https://orcid.org/0000-0002-4404-0456

References

Ackerman, A. S., & Marley, M. S. 2001, ApJ, 556, 872
Ackerman, A. S., Toon, O. B., & Hobbs, P. V. 1995, JGR, 100, 7121
Allard, F., Hauschildt, P. H., Alexander, D. R., Tamanai, A., & Schweitzer, A. 2001, ApJ, 556, 357
Astropy Collaboration, Robitaille, T. P., & Tollerud, E. J. 2013, A&A, 558, A33
Bailer-Jones, C. A. L., & Mundt, R. 2001, A&A, 367, 218
Begemann, B., Dorschner, J., Henning, T., et al. 1997, ApJ, 476, 199
Brande, J., Barclay, T., Schlieder, J. E., Lopez, E. D., & Quintana, E. V. 2020, AJ, 159, 18
Bryan, M. L., Chiang, E., Bowler, B. P., et al. 2020, AJ, 159, 181
Buras, R., Dowling, T., & Emde, C. 2011, JQSRT, 112, 2028

Burningham, B., Faherty, J. K., Gonzales, E. C., et al. 2021, MNRAS, 506, 1944
Burningham, B., Marley, M. S., Line, M. R., et al. 2017, MNRAS, 470, 1177
Burrows, A., Marley, M., Hubbard, W. B., et al. 1997, ApJ, 491, 856
Burrows, A., & Sharp, C. M. 1999, ApJ, 512, 843
Burrows, A., Sudarsky, D., & Hubbard, W. B. 2003, ApJ, 594, 545
Burrows, A., Sudarsky, D., & Hubeny, I. 2006, ApJ, 650, 1140
Carnall, A. C. 2017, arXiv:1705.05165
Chabrier, G., & Baraffe, I. 2000, ARA&A, 38, 337
Cushing, M. C., Marley, M. S., Saumon, D., et al. 2008, ApJ, 678, 1372
Cushing, M. C., Roellig, T. L., Marley, M. S., et al. 2006, ApJ, 648, 614
Danielski, C., Baudino, J.-L., Lagage, P.-O., et al. 2018, AJ, 156, 276
Dorschner, J., Begemann, B., Henning, T., Jaeger, C., & Mutschke, H. 1995, A&A, 300, 503
Fabian, D., Henning, T., Jäger, C., et al. 2001, A&A, 378, 228
Faherty, J. K., Burgasser, A. J., Cruz, K. L., et al. 2009, AJ, 137, 1
Fortney, J. J., Marley, M. S., Saumon, D., & Lodders, K. 2008, ApJ, 683, 1104
Freedman, R. S., Lustig-Yaeger, J., Fortney, J. J., et al. 2014, ApJS, 214, 25
Freedman, R. S., Marley, M. S., & Lodders, K. 2008, ApJS, 174, 504
Gao, P., & Benneke, B. 2018, ApJ, 863, 165
Gao, P., Marley, M. S., & Ackerman, A. S. 2018, ApJ, 855, 86
Gao, P., Wakeford, H. R., Moran, S. E., & Parmentier, V. 2021, JGRE, 126, e06655
Gelino, C. R., Marley, M. S., Holtzman, J. A., Ackerman, A. S., & Lodders, K. 2002, ApJ, 577, 433
Hansen, J. E., & Travis, L. D. 1974, SSRv, 16, 527
Helling, C., Dehn, M., Woitke, P., & Hauschildt, P. H. 2008a, ApJL, 675, L105
Helling, C., Thi, W. F., Woitke, P., & Fridlund, M. 2006, A&A, 451, L9
Helling, C., & Woitke, P. 2006, A&A, 455, 325
Helling, C., Woitke, P., & Thi, W.-F. 2008b, A&A, 485, 547
Henning, T., & Mutschke, H. 1997, A&A, 327, 743
Hiranaka, K., Cruz, K. L., Douglas, S. T., Marley, M. S., & Baldassare, V. F. 2016, ApJ, 830, 96
Jäger, C., Dorschner, J., Mutschke, H., Posch, T., & Henning, T. 2003, A&A, 408, 193
Jäger, C., Molster, F. J., Dorschner, J., et al. 1998, A&A, 339, 904
Kirkpatrick, J. D. 2005, ARA&A, 43, 195
Kitzmann, D., & Heng, K. 2018, MNRAS, 475, 94
Koike, C., Kaito, C., Yamamoto, T., et al. 1995, Icar, 114, 203
Line, M. R., Teske, J., Burningham, B., Fortney, J. J., & Marley, M. S. 2015, ApJ, 807, 183
Lodders, K. 2002, ApJ, 577, 974
Lodders, K., & Fegley, B. 2006, Astrophysics Update 2 (Springer Praxis Books) (Berlin: Springer)
Looper, D. L., Kirkpatrick, J. D., Cutri, R. M., et al. 2008, ApJ, 686, 528
Marley, M. S., Ackerman, A. S., Cuzzi, J. N., & Kitzmann, D. 2013, in Clouds and Hazes in Exoplanet Atmospheres, ed. S. J. Mackwell et al. (Tucson, AZ: Univ. Arizona Press), 367
Marley, M. S., Gelino, C., Stephens, D., Lunine, J. I., & Freedman, R. 1999, ApJ, 513, 879
Marley, M. S., & Robinson, T. D. 2015, ARA&A, 53, 279
Marley, M. S., Saumon, D., Guillot, T., et al. 1996, Sci, 272, 1919
Marley, M. S., Seager, S., Saumon, D., et al. 2002, ApJ, 568, 335
McKay, C. P., Pollack, J. B., & Courtin, R. 1989, Icar, 80, 23
Metchev, S. A., Heinze, A., Apai, D., et al. 2015, ApJ, 799, 154
Morley, C. V., Fortney, J. J., Marley, M. S., et al. 2012, ApJ, 756, 172
Morley, C. V., Fortney, J. J., Marley, M. S., et al. 2015, ApJ, 815, 110
Morley, C. V., Marley, M. S., Fortney, J. J., et al. 2014, ApJ, 787, 78
Mutschke, H., & Mohr, P. 2019, A&A, 625, A61
Palik, E. D. 1985, Academic Press Handbook Series (New York: Academic Press)
Pontoppidan, K. M., Pickering, T. E., Laidler, V. G., et al. 2016, Proc. SPIE, 9910, 991016
Posch, T., Kerschbaum, F., Fabian, D., et al. 2003, ApJS, 149, 437
Powell, D., Louden, T., Kreidberg, L., et al. 2019, ApJ, 887, 170
Powell, D., Zhang, X., Gao, P., & Parmentier, V. 2018, ApJ, 860, 18
Radigan, J., Lafrenière, D., Jayawardhana, R., & Artigau, E. 2014, ApJ, 793, 75
Saumon, D., & Marley, M. S. 2008, ApJ, 689, 1327
Sebastian, D., Gillon, M., Ducrot, E., et al. 2021, A&A, 645, A100
Stamnes, K., Tsay, S.-C., Jayaweera, K., & Wiscombe, W. 1988, ApOpt, 27, 2502
Stephens, D. C., Leggett, S. K., Cushing, M. C., et al. 2009, ApJ, 702, 154
Steyer, T. R. 1974, PhD thesis, Univ. Arizona
Toon, O. B., Turco, R. P., Westphal, D., Malone, R., & Liu, M. S. 1988, JAtS, 45, 2123
Tsuji, T., Ohnaka, K., Aoki, W., & Nakajima, T. 1996, A&A, 308, L29
Turco, R. P., Hamill, P., Toon, O. B., Whitten, R. C., & Kiang, C. S. 1979, JAtS, 36, 699
Ueda, K., Yanagi, H., Noshiro, R., Hosono, H., & Kawazoe, H. 1998, JPCM, 10, 3669
van de Hulst, H. C. 1957, Light Scattering by Small Particles (New York: Wiley)
Visscher, C., Lodders, K., & Fegley, B. J. 2006, ApJ, 648, 1181
Visscher, C., Lodders, K., & Fegley, B., Jr. 2010, ApJ, 716, 1060
Vos, J. M., Biller, B. A., Allers, K. N., et al. 2020, AJ, 160, 38
Vos, J. M., Biller, B. A., Bonavita, M., et al. 2019, MNRAS, 483, 480
Wakeford, H. R., Visscher, C., Lewis, N. K., et al. 2017, MNRAS, 464, 4247
Wetzel, S., Klevenz, M., Gail, H. P., Pucci, A., & Trieloff, M. 2013, A&A, 553, A92
Zeidler, S., Mutschke, H., & Posch, T. 2015, ApJ, 798, 125
Zeidler, S., Posch, T., & Mutschke, H. 2013, A&A, 553, A81